



# Mechanistic origins of the high-pressure inhibition of methanol dehydration rates in small-pore acidic zeolites



John R. Di Iorio<sup>a</sup>, Alexander J. Hoffman<sup>b</sup>, Claire T. Nimlos<sup>a</sup>, Steven Nystrom<sup>b</sup>, David Hibbitts<sup>b,\*</sup>, Rajamani Gounder<sup>a,\*</sup>

<sup>a</sup> Charles D. Davidson School of Chemical Engineering, Purdue University, 480 Stadium Mall Drive, West Lafayette, IN 47907, USA

<sup>b</sup> Department of Chemical Engineering, University of Florida, 1030 Center Drive, Gainesville, FL 32611, USA

## ARTICLE INFO

### Article history:

Received 7 August 2019

Revised 26 September 2019

Accepted 5 October 2019

Available online 31 October 2019

### Keywords:

Methanol dehydration

Reactant inhibition

Chabazite

Zeolite

Heterogeneous catalysis

## ABSTRACT

Turnover rates of Brønsted acid-catalyzed methanol dehydration to dimethyl ether become inhibited at high methanol pressures (>10 kPa, 415 K) on small-pore zeolites (CHA, AEI, LTA, LEV), irrespective of the distribution of framework Al and their attendant H<sup>+</sup> sites, but not on medium-pore or large-pore zeolites. High-pressure kinetic inhibition occurs concomitantly with the stabilization of higher-order methanol clusters (e.g., trimers, tetramers) observed experimentally by physisorption of liquid-like methanol and the appearance of vibrational modes for methanol clusters in IR spectra, consistent with the attenuation of such inhibition at higher temperatures (>450 K) that result in decreased methanol coverage. DFT-predicted methanol coverage phase diagrams confirm that higher-order methanol clusters form in pressure and temperature ranges corresponding to the onset of kinetic inhibition observed experimentally, and that higher-order methanol clusters are reactive but that excess methanol increases the apparent barriers to form kinetically relevant transition states that eliminate dimethyl ether and thus inhibit turnover rates. This combined experimental and theoretical investigation provides precise mechanistic interpretation of the high-pressure inhibition of methanol dehydration turnover rates on small-pore Brønsted acid zeolites. This rigorous analysis enables the development of kinetic models to account for the diverse structures of methanol precursors that dehydrate to form dimethyl ether, and methods to assess the prevalence of higher-order clusters that serve as reactive and inhibitory intermediates within small-pore zeolites during methanol conversion.

© 2019 Elsevier Inc. All rights reserved.

## 1. Introduction

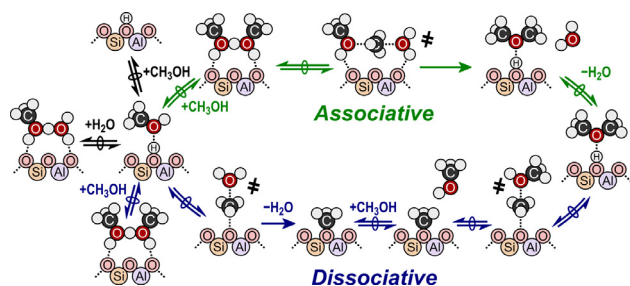
Methanol is a promising carbon source for producing light olefins (e.g., ethene, propene) and aromatics over acidic zeolite catalysts at elevated temperatures (>453 K) via the methanol-to-olefins (MTO) and methanol-to-gasoline (MTG) processes [1,2], in which product selectivities can be tuned via judicious choice of reaction conditions (e.g., temperature, methanol pressure) [3] and zeolite framework [3–5]. The conversion of methanol into olefins proceeds through a “hydrocarbon pool” mechanism, wherein methanol is dehydrated at Brønsted acid sites to form methoxy intermediates that subsequently react with confined polymethylated aromatics to generate new C–C bonds [3,4,6]. Surface-bound methoxy groups (CH<sub>3</sub>–Z), formed via methanol dehydration, have also been implicated in the initiation of C–C

bond formation, at low turnover numbers, via carbonylation with either carbon monoxide or formaldehyde present either as impurities or formed during reaction [6–8]. Methanol dehydration to dimethyl ether (DME) occurs selectively without olefin formation at low-temperatures (<453 K) [9,10], and measurement of methanol dehydration rate constants has enabled investigating the individual effects of confinement and acid strength in zeolite acid catalysis [10–12].

Methanol dehydration to DME on solid Brønsted acids can proceed via two different mechanisms, referred to as the associative (concerted) or dissociative (sequential) mechanisms (Scheme 1) [10–14]. The first step in both mechanisms is quasi-equilibrated adsorption of a gas-phase methanol at a bare proton. In the associative mechanism, protonated methanol dimers form via quasi-equilibrated adsorption of a second gas-phase methanol, and then eliminate DME and water in a kinetically relevant dehydration step (Scheme 1, top). The dissociative mechanism (Scheme 1, bottom), in contrast, involves kinetically relevant dehydration of methanol monomers to eliminate water and form a surface-bound methoxy

\* Corresponding authors.

E-mail addresses: [hibbitts@ufl.edu](mailto:hibbitts@ufl.edu) (D. Hibbitts), [rgounder@purdue.edu](mailto:rgounder@purdue.edu) (R. Gounder).



**Scheme 1.** Structures of intermediates and transition states (marked as †) for the associative (top path) and dissociative (bottom path) mechanisms of Brønsted acid-catalyzed methanol dehydration to DME.

intermediate. Surface methoxy intermediates then undergo nucleophilic attack by a second gas-phase methanol in a quasi-equilibrated step to form DME. DME formation rates via the dissociative mechanism are thus inhibited by the formation of protonated methanol dimers [10], while methanol-water complexes can inhibit both pathways (Scheme 1).

Measured reaction kinetics (433 K) and DFT calculations indicate that methanol dehydration to DME proceeds via the associative mechanism at Brønsted acid sites ( $H^+$  sites) of polyoxometalate clusters (POM) supported on amorphous  $SiO_2$  [10], and at such sites confined within medium-pore and large-pore zeolites (FAU, SFH, BEA, MOR, MTW, MFI, and MTT, 0.5–1.2 nm diameter voids) [11–13,15]. Turnover rates of methanol dehydration (433 K, per  $H^+$ ) on these catalysts follow a Langmuirian dependence on methanol partial pressure (0.05–20 kPa), transitioning from a first-order to zero-order kinetic regime at high methanol pressures. Additionally, *in situ* IR spectra measured on MFI zeolites (433 K, 0.1–16 kPa  $CH_3OH$ ) do not show bare protons or surface methoxy intermediates, consistent with the associative mechanism [13] and suggesting that all sites are covered by methanol monomers or higher order clusters during reaction. Turnover rates (per  $H^+$ , 415 K) measured on small-pore CHA zeolites ( $Si/Al = 15$ ) containing isolated  $H^+$  sites also appear to proceed via the associative mechanism, based on analogous observations from kinetic and *in situ* IR data (0.05–20 kPa  $CH_3OH$ , 415 K) [16]. *In situ* IR spectra (0.05–20 kPa  $CH_3OH$ , 415 K) of CHA zeolites of similar composition ( $Si/Al = 15$ ) containing paired  $H^+$  sites (2 Al per 6-MR), however, show surface methoxy present at coverages that increase with the fraction of paired  $H^+$  sites [16], suggesting that the dissociative dehydration mechanism may proceed at paired  $H^+$  sites in CHA. Furthermore, turnover rates (per  $H^+$ ) on CHA increase with the fraction of  $H^+$  sites in paired configurations [16,17], and density functional theory (DFT) calculations suggest that interactions between proximal Brønsted acid sites may alter the stability of the deprotonated conjugate base and lead to an increase in acid strength [18]. The precise mechanistic roles of paired and isolated  $H^+$  site ensembles in CHA, however, are convoluted by inhibition of methanol dehydration rates at high methanol pressures (415 K, >10 kPa  $CH_3OH$ ) [16], a phenomenon not observed on medium-pore and large-pore zeolites [11,13].

The inhibition of certain alkanol dehydration mechanisms has been previously reported for  $C_2$ – $C_4$  alkanols over solid acid catalysts. Bimolecular dehydration rates of ethanol to form diethyl ether (MFI, FER, MOR; 368–409 K, >6 kPa  $C_2H_5OH$ ) [19] and propanol dehydration to dipropyl ether (MFI, 413–443 K, <4 kPa  $C_3H_7OH$ ) [20] asymptotically approach a zero-order dependence and are not inhibited at higher alkanol partial pressures, similar to reports of methanol dehydration rates on medium-pore and large-pore zeolites [11]. Ethanol and propanol, unlike methanol, are also able to undergo unimolecular dehydration to form the

corresponding alkene. Ethanol dehydration to ethene is inhibited on MOR zeolites (368–409 K, <6 kPa  $C_2H_5OH$ ) because additional ethanol molecules adsorb at ethanol monomers and must desorb prior to ethene formation transition states [19]. Similar observations have also been reported for unimolecular dehydration of propanol to propene (MFI, 413–443 K, <4 kPa  $C_3H_7OH$ ) [20] and butanol to butene (W-POM/ $SiO_2$ , 343 K, <1 kPa  $C_4H_9OH$ ) [21] because the coordination of a second alkanol or water forms dimeric intermediates that are spectators in alkene formation routes. These observations indicate that unimolecular alkanol dehydration to the corresponding alkene (<443 K,  $C_2$ – $C_4$  alkanols) is inhibited by coordination of a second alkanol molecule to form higher molecularity intermediates that behave as spectators, but that such intermediates can condense to eliminate the corresponding dialkyl ether and water at rates (<443 K,  $C_1$ – $C_4$  alkanols) that approach a zero-order kinetic regime at high alkanol partial pressures.

Thus, the high-pressure inhibition of bimolecular methanol dehydration rates (415 K) in small-pore CHA zeolites presents a sharp contrast to the inhibition of only unimolecular alkanol dehydration in medium-pore and large-pore zeolites, and the precise mechanistic origin of this inhibition has remained imprecisely understood. In our prior work, such high-pressure rate inhibition was accounted for by including an elementary step for the formation of an unreactive methanol trimer via quasi-equilibrated adsorption of a methanol at a protonated dimer, to derive an *ad hoc* rate equation that allowed estimating first-order and zero-order rate constants from experimentally measured rate data on CHA zeolites [16]. Here, we further investigate the formation and stability of different methanol species at isolated  $H^+$  sites in CHA zeolites during methanol dehydration catalysis using a combination of kinetic, spectroscopic, and theoretical probes. High-pressure inhibition of methanol dehydration rates (per  $H^+$ ) becomes attenuated at elevated reaction temperatures (>450 K), which coincides with the disappearance of IR vibrational bands characteristic of methanol trimers and larger clusters ( $\sim 3370\text{ cm}^{-1}$ ) detected by *in situ* IR spectroscopy (343–473 K, 10 kPa  $CH_3OH$ ). Methanol adsorption isotherms indicate that the onset of dehydration rate inhibition (415 K, per  $H^+$ ) occurs at coverages corresponding to >2  $CH_3OH$  per  $H^+$  site, consistent with IR spectra (0.01–3  $CH_3OH/H^+$ ; 293 K) that show the appearance of methanol clusters at coverages of >0.7  $CH_3OH$  per  $H^+$  site and that increase in intensity with increasing methanol coverage. DFT is used to calculate the Gibbs free energies of various methanol complexes (1–12  $CH_3OH$  per proton) confined within CHA as a function of temperature and methanol pressure, which indicate that methanol trimers are preferentially stabilized in CHA at methanol pressures corresponding to the onset of kinetic inhibition observed experimentally (>10 kPa, 415 K). Apparent free energy barriers for methanol dehydration are calculated considering up to four methanol-derived species at an  $H^+$  site, in which spectating methanol species are found to insert between reacting species and framework O atoms. DFT-predicted methanol dehydration rates (415 K) are compared with experimental data to determine plausible reaction mechanisms and highlight the critical influence of the zeolite framework on stabilizing reactive and inhibitory intermediates in methanol conversion pathways.

## 2. Methods and materials

### 2.1. Catalyst synthesis and characterization

#### 2.1.1. Synthesis of different small-pore zeolites

The full synthesis procedure of CHA zeolites containing isolated  $H^+$  sites is described in detail elsewhere [17]. In brief, CHA was syn-

thesized using N,N,N-trimethyl-1-adamantylammonium hydroxide as the structure directing agent (SDA) with a molar ratio in the crystallization medium of 1 SiO<sub>2</sub>/0.033 Al<sub>2</sub>O<sub>3</sub>/0.5 TMAOH/44 H<sub>2</sub>O. In a typical synthesis, deionized water and an aqueous solution of TMAOH were mixed and stirred for 15 min under ambient conditions in a perfluoroalkoxy alkane (PFA) jar. Next, aluminum hydroxide powder was added and stirred for 15 min under ambient conditions. Finally, an aqueous colloidal silica solution was added and the contents were covered and stirred for 2 h under ambient conditions. The resulting mixture was transferred to a PTFE-lined stainless-steel autoclave and heated to 433 K under rotation at 40 RPM for 6 days.

The full synthesis procedure of AEI zeolites and the organic SDA, cis-2,6-dimethylpiperidinium hydroxide (DMPOH), are described in detail elsewhere [22,23]. Briefly, AEI was synthesized using a molar composition of 1 SiO<sub>2</sub>/0.017 Al<sub>2</sub>O<sub>3</sub>/0.07 DMPOH/0.58 NaOH/12.3 H<sub>2</sub>O. The resulting solution was transferred to a PTFE-lined stainless-steel autoclave and heated to 413 K under rotation for 4 days.

LEV zeolites were synthesized following a reported procedure using a mixture of 1-adamantylamine (AdANH<sub>2</sub>) and sodium fluoride [24]. A molar ratio of 1 SiO<sub>2</sub>/0.024 Al<sub>2</sub>O<sub>3</sub>/0.3 AdANH<sub>2</sub>/0.05 NaF/10 H<sub>2</sub>O was used in the crystallization medium. In a PFA jar, 4.455 g of AdANH<sub>2</sub> (Sigma-Aldrich, 97 wt%) were added to 17.081 g of deionized water (18.2 MΩ) and stirred until fully dissolved. 6 g of FAU zeolite (CBV720, Si/Al = 21, Zeolyst) were added and stirred for 10 min until a uniform slurry was obtained. Finally, 0.237 g of NaF (Sigma-Aldrich, 99 wt%) were added and the mixture was covered and stirred for 2 h at ambient temperature. The resulting mixture was then loaded into a 45 cm<sup>3</sup> PTFE-lined stainless-steel autoclave and placed in a static oven at 423 K for 10 days.

LTA zeolites and the required organic SDA, 1,2-dimethyl-3-(4-methylbenzyl)imidazolium hydroxide (DMMBI-OH) were synthesized according to previous reports [25]. The synthesis of DMMBI-Cl was carried out in a two-neck 500 cm<sup>3</sup> round-bottom flask attached to a water-cooled condenser to minimize solvent evaporation. In the round-bottom flask, a 0.1 M solution of 1,2-dimethylimidazole (Sigma-Aldrich, 98 wt%) was first prepared by dissolving 0.48 g of 1,2-dimethylimidazole in 50 cm<sup>3</sup> of chloroform (Sigma-Aldrich, 99.8 wt%) and stirring for 15 min to homogenize the contents. In a separate 100 cm<sup>3</sup> pear-shaped flask, a 0.1 M solution of 4-methylbenzyl chloride (Sigma-Aldrich, 98 wt%) was prepared by adding 0.70 g of 4-methylbenzyl chloride to 50 cm<sup>3</sup> of chloroform and stirring until homogenous. The 0.1 M solution of 4-methylbenzyl chloride was then added to the 0.1 M solution of 1,2-dimethylimidazole, the second-neck of the round-bottom flask capped with a Viton septum, and stirred for two days at 303 K. After two days, the solution was evaporated, dissolved in a minimum amount of chloroform, and then recrystallized with diethyl ether (Sigma-Aldrich, 99 wt%). A portion of the crystalline product was dissolved in D<sub>2</sub>O (Cambridge Isotope Laboratories, 99.9%) and a <sup>1</sup>H NMR spectrum was recorded and was consistent with reported <sup>1</sup>H chemical shifts for DMMBI-Cl (details in Supp. Info.) [25]. The resulting Cl<sup>-</sup> form of the SDA salt was then converted to its OH<sup>-</sup> form by ion-exchange with a Dowex Marathon A (Sigma-Aldrich) using a mass ratio of 1 SDA/3 resin/5 H<sub>2</sub>O and repeated thrice with fresh resin. A final purity of ~80% DMMBI-OH was confirmed by titration with a 0.1 M HCl solution.

The synthesis of high-silica LTA zeolites was performed using a mixture of DMMBI-OH and tetramethylammonium hydroxide (TMAOH) as the SDAs with a molar composition of 1 SiO<sub>2</sub>/0.025 Al<sub>2</sub>O<sub>3</sub>/0.45 DMMBI-OH/0.05 TMAOH/0.49 HF/5 H<sub>2</sub>O in the synthesis medium. In a PFA jar, 11.040 g of an aqueous DMMBI-OH solution (20 wt%) were added to 0.233 g of an aqueous TMAOH solution (Sigma-Aldrich, 25 wt%) and stirred for five minutes. Next,

0.032 g of Al(OH)<sub>3</sub> powder (SPI Pharma) were added to the SDA solution and stirred until fully dissolved. 1.746 g of tetraethylorthosilicate (TEOS, Sigma-Aldrich, 98 wt%) were then added and the resulting mixture was capped and stirred for two hours under ambient conditions. After two hours, the mixture was uncapped and excess water and ethanol, formed upon hydrolysis of TEOS, was allowed to evaporate under ambient conditions until the target H<sub>2</sub>O/SiO<sub>2</sub> ratio was obtained. 5 g of additional water were then added and the mixture was again dehydrated to reach the target H<sub>2</sub>O/SiO<sub>2</sub> ratio. After this second dehydration step, 0.160 g of hydrofluoric acid (Sigma-Aldrich, 48 wt%, 99.999% trace metals basis) were added dropwise and stirred with a PTFE spatula for 15 min. The synthesis mixture was then transferred to a 23 cm<sup>3</sup> PTFE-lined stainless-steel autoclave and heated to 448 K under rotation (60 RPM) for 7 days.

After crystallization of each zeolite, the solid products were washed repeatedly with acetone (Sigma-Aldrich, 99.9 wt%) and deionized water (35 cm<sup>3</sup> g<sub>cat</sub><sup>-1</sup>) until the pH of the supernatant remained constant between washes, recovered via centrifugation, and dried at 373 K overnight under stagnant air. The dried, as-synthesized zeolites were then heated to 853 K (0.0167 K s<sup>-1</sup>) under flowing air (1.67 cm<sup>3</sup> g<sub>cat</sub><sup>-1</sup> s<sup>-1</sup>) for 10 h to remove the occluded organic SDA.

**2.1.1.1. <sup>1</sup>H NMR of 1,2-Dimethyl-3-(4-methylbenzyl)imidazolium chloride.** After crystallization of DMMBI-Cl, approximately 0.5 g of the recovered solid were dissolved in 0.5 cm<sup>3</sup> of D<sub>2</sub>O and a portion of this solution was placed inside an NMR tube (Wilmad Lab-Glass, 5 mm thin wall, 7 in., 500 MHz) for <sup>1</sup>H NMR analysis. NMR spectra were collected on a Bruker ARX500 spectrometer equipped with a 5 mm BBFO Z-gradient probe at ambient temperature and represent the average of 128 scans. The measured spectrum is shown in Fig. S.9 of the Supp. Info. <sup>1</sup>H NMR (D<sub>2</sub>O, 500 MHz): δ 7.31 (s, 2H), 7.27 (d, 2H), 7.18 (d, 2H), 5.27 (s, 2H), 3.74 (s, 3H), 2.54 (s, 3H), 2.31 (s, 3H).

### 2.1.2. Structural characterization of zeolite topology and porosity

The crystal topology of all synthesized zeolites was determined from powder X-ray diffraction (XRD) patterns measured on a Rigaku Smartlab X-ray diffractometer equipped with a Cu Kα radiation source (λ = 0.154 nm) operated at 1.76 kW. Samples were loaded onto zero-background sample holders (Rigaku) and pressed flat using a microscope slide prior to collecting diffraction patterns from 2θ = 4–40° at a rate of 0.04° s<sup>-1</sup> and a step size of 0.01°. Crystal topologies were confirmed by comparison of experimental diffraction patterns with those reported in the International Zeolite Association (IZA) structure database [26]. XRD patterns are shown in Fig. S.10 of the Supp. Info.

Zeolite micropore volumes were determined from Ar adsorption isotherms measured in a liquid Ar bath (87 K) on a Micromeritics ASAP 2020 Surface Area and Porosity Analyzer. Typically, 0.03–0.05 g of sieved zeolite (nominal diameter of 180–250 μm) were degassed by first heating to 393 K (0.167 K s<sup>-1</sup>) under vacuum (<5 × 10<sup>-6</sup> torr) for 2 h before further heating to 623 K (0.167 K s<sup>-1</sup>) under vacuum (<5 × 10<sup>-6</sup> torr) and holding for 9 h. The volume of gas adsorbed (cm<sup>3</sup> g<sub>cat</sub><sup>-1</sup> at STP) was estimated from a semi-log derivative plot of the adsorption isotherm (∂(V<sub>ads</sub>)/∂(ln(P/P<sub>0</sub>)) vs. ln(P/P<sub>0</sub>)). Ar adsorption isotherms are shown in Fig. S.11 and micropore volumes are tabulated in Table S.1 of the Supp. Info.

### 2.1.3. Elemental analysis and titration of H<sup>+</sup> sites using NH<sub>3</sub>

Total Al and H<sup>+</sup> site contents are tabulated in Table S.1 of the Supp. Info. The total Al content of each zeolite was determined from atomic absorption spectroscopy (AAS) using a Perkin Elmer AAnalyst 300 Atomic Absorption Spectrometer. After removal of

occluded organic SDA molecules by oxidative treatment (853 K, 10 h), zeolite samples (~0.02 g) were digested in 3 g of HF acid (48 wt%, Sigma Aldrich) overnight (at least 8 h) and then diluted with 50 g of deionized water (18.2 MΩ). Aqueous solutions were nebulized into an acetylene/nitrous oxide flame and Al absorbances were measured at a wavelength of 309.3 nm. Al concentrations were determined from calibration curves generated from solutions of known composition prepared by dilution of a 1000 ppm Al standard (Sigma-Aldrich, TraceCERT).

The number of H<sup>+</sup> sites on each zeolite catalyst was measured by temperature programmed desorption (TPD) of NH<sub>3</sub> using reported procedures [27]. After organic removal, zeolite samples were exposed to a 1 M aqueous NH<sub>4</sub>NO<sub>3</sub> (Sigma-Aldrich, 99 wt%) solution (150 cm<sup>3</sup> g<sub>cat</sub><sup>-1</sup>) and stirred under ambient conditions for 24 h. Solids were then washed six times with deionized water (35 cm<sup>3</sup> g<sub>cat</sub><sup>-1</sup>), recovered via centrifugation, and dried overnight at 373 K under stagnant air. NH<sub>4</sub>-exchanged zeolite samples were then pelletized and sieved (nominal diameter of 180–250 μm) and suspended between two quartz wool plugs in a quartz U-tube reactor. The quartz reactor was then loaded into a Micromeritics Autochem II 2920 Chemisorption analyzer and heated to 873 K (0.167 K s<sup>-1</sup>) under flowing He (50 cm<sup>3</sup> g<sub>cat</sub><sup>-1</sup> s<sup>-1</sup>, 99.999%, Indiana Oxygen). The total amount of NH<sub>3</sub> desorbed was then quantified using an Agilent 5973 N mass selective detector (MSD).

## 2.2. Methanol dehydration kinetics and reactor configuration

Methanol dehydration kinetics were measured in a tubular packed-bed quartz reactor (7 mm inner diameter) with plug-flow hydrodynamics as described previously [16]. Zeolite samples were pelleted and sieved (nominal diameter between 180 and 250 μm) and supported between two quartz wool plugs in the reactor. The total amount of catalyst loaded into the reactor was varied between 0.005 and 0.030 g to maintain differential conversions. The total mass of zeolite charged to the reactor was maintained at a minimum of 0.025 g by dilution with Si-CHA. Dilutions (2–10 × dilution ratio) were prepared by grinding together both powders in a mortar and pestle, pelletizing, and then crushing to retain particles between 180 and 250 μm. Reactors were placed inside a three-zone furnace (Series 3210, Applied Test Systems) with a K-type thermocouple placed in direct contact with the external surface of reactor at the center of the catalyst bed and the temperature of the catalyst bed was controlled by Watlow controllers (EZ-Zone Series). Prior to contact with reactant mixtures, zeolite catalysts were heated to 773 K (0.033 K s<sup>-1</sup>) and held for 4 h under a 5% O<sub>2</sub>/He flow (50 cm<sup>3</sup> g<sub>cat</sub><sup>-1</sup> s<sup>-1</sup>, 99.999%, Indiana Oxygen). Upon cooling to the desired reaction temperature, samples were flushed with He (150 cm<sup>3</sup> g<sub>cat</sub><sup>-1</sup> s<sup>-1</sup>, 99.999%, Indiana Oxygen) for 0.5 h to remove residual O<sub>2</sub>. Methanol (99.9 wt%, Sigma-Aldrich) was introduced into the He gas stream using a syringe pump (Legato 100, KD Scientific) and sent to the reactor through heated stainless-steel lines maintained at > 373 K using resistive heating tape (Brisk Heat Co.) and insulating wrap. Concentrations of reactants and products were measured using an Agilent 6890 gas chromatograph equipped with a flame ionization detector and an HP Plot-Q column (0.53 mm ID × 30 m × 40 μm film, Agilent). Methane (25% CH<sub>4</sub>/Ar, 99.999%, Indiana Oxygen) was used as an internal standard and introduced into the reactor effluent at a constant rate (0.083 cm<sup>3</sup> s<sup>-1</sup>).

Apparent first-order and zero-order methanol dehydration free energy barriers were measured on CHA zeolites with isolated H<sup>+</sup> sites from DME formation rates (per H<sup>+</sup>) measured as a function of methanol pressure (0.05–50 kPa) at temperatures varied non-systematically between 383 and 415 K. Apparent first and zero-order methanol dehydration rate constants (per H<sup>+</sup>) were deter-

mined from a least squares regression of Eq. (4) to the rate data and the Eyring-Polanyi equation was used to extract first and zero-order apparent activation enthalpies and entropies. These data and calculations are shown in Section S.10 of the Supp. Info.

## 2.3. Measurement of IR spectra

### 2.3.1. Steady-state methanol dehydration

IR spectra collected under steady-state methanol dehydration catalysis were measured on a Nicolet 4700 spectrometer with an HgCdTe detector (MCT, cooled to 77 K by liquid N<sub>2</sub>). Spectra were collected between 4000 and 400 cm<sup>-1</sup> and averaged over 64 scans at a 2 cm<sup>-1</sup> resolution and referenced to an empty cell background collected under He flow (0.33 cm<sup>3</sup> s<sup>-1</sup>, 99.999%, Indiana Oxygen) at 415 K. Zeolite catalysts were pressed into self-supporting wafers (0.01–0.02 g<sub>cat</sub> cm<sup>-2</sup>) and placed within a custom-built quartz IR cell sealed with CaF<sub>2</sub> windows [16,28,29]. Temperatures were measured by K-type thermocouples (Omega) held ~2 mm from each side of the zeolite wafer. Prior to each measurement, the zeolite wafer was heated to 773 K (0.083 K s<sup>-1</sup>) for 4 h under flowing air (13.3 cm<sup>3</sup> g<sub>cat</sub><sup>-1</sup> s<sup>-1</sup>) purified by a purge gas generator (Parker Balston, <1 ppm of CO<sub>2</sub>, 200 K H<sub>2</sub>O dew point), and then cooled under flowing He (13.3 cm<sup>3</sup> g<sub>cat</sub><sup>-1</sup> s<sup>-1</sup>) to the analysis temperature. Methanol (Sigma-Aldrich, 99.9 wt%) was introduced to the quartz IR cell (0.1–22 kPa) by a syringe pump (Legato 100, KD Scientific) connected to stainless-steel transfer lines maintained >353 K using resistive heating tape (Brisk Heat Co.) and insulating wrap. IR spectra were recorded as a function of time until peak intensities remained constant for >0.25 h. All spectra were baseline corrected and normalized to the zeolite combination and overtone T-O-T vibrational modes (1750–2100 cm<sup>-1</sup>) of the freshly dehydrated zeolite spectrum.

### 2.3.2. IR spectra measured at known methanol coverages

Methanol adsorption isotherms were measured on the same IR apparatus as described in Section 2.3.1, except a custom-built glass vacuum manifold was used to introduce small amounts (<1 torr doses) of methanol onto dehydrated CHA zeolites [28,29]. IR spectra taken during methanol adsorption isotherms were referenced to an empty cell background taken under dynamic vacuum at 293 K. Prior to methanol dosing experiments, zeolite self-supporting wafers were heated to 773 K (0.083 K s<sup>-1</sup>) under dynamic vacuum (<0.1 torr) for 2 h before cooling to room temperature. The adsorption temperature was maintained below room temperature (293 K) using a closed-loop chiller that recirculated chilled water (288 K) through cooling coils encircling the quartz IR cell [28]. Methanol was loaded into a glass ampule (1/4" OD) and purified on the vacuum manifold via successive freeze-pump-thaw cycles until dissolved gases were no longer observed bubbling out upon thawing. Zeolite samples were exposed to small amounts of methanol (2.5 × 10<sup>-7</sup> mol per dose) and allowed to equilibrate for two minutes prior to measurement of an IR spectrum. Methanol coverages were calculated as the total number of moles of methanol that disappeared from the gas phase during each dose by taking the difference in the initial and final number of moles in the gas phase.

## 2.4. Measurement of methanol adsorption isotherms

High-resolution methanol adsorption isotherms were measured at 293 K using the same gas adsorption apparatus as described in Section 2.1.2. Methanol adsorbates (Sigma-Aldrich, 99.9%) were degassed by successive freeze-pump-thaw cycles and supplied at their respective vapor pressures at 293 K. Adequate resolution at low pressures was achieved by holding samples under dynamic vacuum (<5 × 10<sup>-6</sup> torr) on the analysis port during the prepara-

tion sequence until the dosing manifold was charged with adsorbate prior to collection of the first data point. Methanol was then dosed onto the evacuated zeolite sample in equilibrated increments of  $1 \text{ cm}^3 \text{ g}^{-1}$  (gas volume adsorbed at STP per gram) until a final relative pressure of  $P/P_0 = 0.6$  was reached. This procedure was previously found necessary for obtaining accurate ethanol and water adsorption isotherms on siliceous BEA zeolites [30]. The full adsorption isotherm is shown in Fig. S.16 in the Supp. Info.

## 2.5. Computational methods

Fully periodic density functional theory (DFT) calculations were performed using the Vienna ab initio software package (VASP) [31–34] and implemented in the Computational Catalysis Interface (CCI) [35]. Planewaves were constructed using the projector augmented wave method (PAW) with an energy cutoff of 400 eV [36,37]. The Brillouin zone was sampled at the  $\Gamma$ -point for all calculations. The Perdew-Burke-Ernzerhof (PBE) form of the generalized gradient approximation (GGA) was used for all calculations [38]. Dispersive interactions were accounted for by including the DFT-D3 empirical correction with Becke and Johnson damping (D3BJ) [39,40]. Structures were optimized in two steps to improve computational efficiency. Structures were optimized in the first step using a wavefunction convergence criteria such that energy variations between iterations were  $<10^{-4}$  eV and forces were computed with a fast Fourier transform (FFT) grid of  $1.5 \times$  the energy cutoff (PREC = .NORMAL. in VASP); structures were relaxed until the maximum force on any atom was  $<0.05 \text{ eV } \text{\AA}^{-1}$ . These settings may result in inaccurate forces near the minimum; as such, structures are then re-optimized with wavefunctions converged to within  $10^{-6}$  eV and forces computed with an FFT grid  $2 \times$  the energy cutoff (PREC = .ACCURATE. in VASP). This two-step optimization scheme has been shown to increase computational efficiency by a factor of  $\sim 3$  for zeolite-based calculations that are sampled at the  $\Gamma$  point [35].

Transition state searches were initiated using the nudged elastic band (NEB) method with 16 intermediate images for each elementary step and converged such that the forces on each atom were  $<0.5 \text{ eV } \text{\AA}^{-1}$  [41,42]. Transition states were then refined starting from these NEB results using the Dimer method [43], where structures were converged using the same criteria as those used for optimizations (energy variation between iterations  $<10^{-6}$  eV, max force per atom  $<0.05 \text{ eV } \text{\AA}^{-1}$ ).

The CHA structure was obtained from the database of the international zeolite association (IZA), with unit cell parameters  $a = b = 13.675 \text{ \AA}$ ,  $c = 14.767 \text{ \AA}$ ,  $\alpha = \beta = 90.0^\circ$ , and  $\gamma = 120.0^\circ$  [26]. The CHA structure is comprised of stacked six-member ring (6-MR) structures with adjacent eight-member ring (8-MR) windows leading into larger cage voids. CHA has one symmetrically unique T-site surrounded by four unique O atoms. One of the 36 Si atoms in the CHA unit cell was replaced by an Al atom (Si/Al = 35) and balanced by a proton to form a Brønsted acid site (Fig. S.1, Supporting Information). Previous work has shown that protons associated with Brønsted acid sites prefer to bind to O1 or O4 atoms and are solvated by 6-MR or 8-MR motifs [18,44].

Zeolites are flexible materials and are prone to restructuring during DFT calculations, as recently emphasized for the MFI framework [45]. Therefore, the unit cell parameters of the CHA unit cell were optimized with an energy cutoff of 800 eV without constraints (ISIF = 3 in VASP) to ensure that these initial unit cell parameters would not result in restructuring. These unit cell parameter optimizations yielded a  $<1\%$  change in each unit cell parameter; therefore, the initial IZA structure was used in all subsequent calculations. Furthermore, annealing of the CHA structure was simulated with *ab initio* molecular dynamics (AIMD) in VASP to confirm that restructuring does not occur with the PBE

exchange-correlation functional and D3BJ correction. The CHA structure was heated from 200 K to 800 K over 3 ps, held at 800 K for 3 ps, and cooled from 800 K to 100 K over 15 ps, each with a timestep of 3 fs. The resulting annealed CHA structure was subsequently optimized using the same convergence criteria described above. This annealed and optimized CHA structure differed by  $<1 \text{ kJ mol}^{-1}$  in energy from the directly optimized CHA structure from the IZA database. Moreover, the two structures differed by a negligible distance. These negligible changes in energy and structure indicate that the CHA structure supplied by IZA is sufficiently stable for kinetic studies.

Vibrational frequency calculations were used to approximate zero-point vibrational energies (ZPVEs), vibrational, rotational, and translational enthalpies ( $H$ ) and free energies ( $G$ ) using a fixed displacement method ( $n = 2$ ) for all gas-phase and adsorbed species. Framework Si and O atoms that were not bound to the Al atom were fixed during frequency calculations within the zeolite framework. These values were used to approximate total enthalpies in conjunction with VASP-derived electronic energies ( $E_0$ ):

$$H = E_0 + ZPVE + H_{vib} + H_{rot} + H_{trans} \quad (1)$$

and free energies

$$G = E_0 + ZPVE + G_{vib} + G_{rot} + G_{trans} \quad (2)$$

at 415 K and 1 bar  $\text{CH}_3\text{OH}$  (standard pressure), the formulas for which are derived from statistical mechanics formalisms (see Section S.1 in the Supp. Info. for details) [46]. All motions for guest species within the zeolite framework are considered vibrations, such that translational and rotational  $H$  and  $G$  are zero for non-gas phase species, which are treated as ideal gases with appropriate equations from statistical mechanics. Enthalpies and entropies ( $S$ ) derived from calculations were used to predict equilibrium constants of adsorption ( $K$ ) from 300 to 500 K, in order to predict adsorption behavior of methanol in CHA and to predict equilibrium and rate constants for DFT-predicted rates. Low-frequency vibrational modes disproportionately contribute to entropy estimates; as such, frequencies below  $60 \text{ cm}^{-1}$  were replaced by  $60 \text{ cm}^{-1}$  (with the exception of the negative frequency in transition states), as in previous work [47,48].

The diverse confining voids within single zeolite frameworks affect the energies of guest species differently depending on the orientation and location of those species [48–50]. Therefore, a systematic method of probing the configurational space of zeolites is critical to find favorable configurations of these intermediates [48]. Here, we perform systematic reorientations on adsorbates and transition states interacting with each O atom of the CHA framework to ensure comprehensive probing of the confining space of the CHA voids. Adsorbates and transition states that strongly interact with framework O atoms (e.g., surface methoxy, transition states forming or breaking C–O bonds, and species H-bonding) were (1) reoriented about the axis formed by the Si and Al bound to the O atom; (2) rotated about their interactions with the framework O above the acid site by changing the adsorbate–O dihedral angle; and (3) moved by altering the angle between the Al, O, and adsorbate. Transition states were rotated about internal bonds and incipient bonds and adsorbates that did not interact strongly with the surrounding framework were rotated about the x-, y-, and z-axes (the y- and z-axes are the same as the b- and c-vectors of the CHA unit cell, respectively). These reorientations yielded structures with large ranges of energies, while preserving strong interactions with the surrounding framework. This further indicates that there are diverse void environments around a single acid site within a zeolite framework, which can be probed using these systematic reorientations [48].

### 3. Results and discussion

#### 3.1. Inhibition of methanol dehydration rates on small-pore zeolites

Methanol dehydration turnover rates (415 K, per  $H^+$ ) on CHA zeolites containing predominantly isolated  $H^+$  sites increase linearly with methanol partial pressure ( $P_{CH_3OH}$ ) at low partial pressures (<1 kPa), before reaching a maximum and transitioning to a kinetic regime reflecting inhibition at high partial pressures (>10 kPa) (Fig. 1). This behavior is not captured by the form of the associative dehydration rate law derived assuming  $H^+$  sites are covered by methanol monomers and protonated dimers as most abundant surface intermediates (MASI) (Eq. (3)) [10].

$$r_A = \frac{k_{DME,A}K_D P_{CH_3OH}}{1 + K_D P_{CH_3OH}} \quad (3)$$

In Eq. (3),  $k_{DME,A}$  is the rate constant for DME formation via the associative mechanism,  $K_D$  is the equilibrium constant for forming a protonated dimer from a gaseous methanol and adsorbed methanol monomer, and  $P_{CH_3OH}$  is partial pressure of methanol. *In situ* IR spectra measured under conditions of methanol dehydration catalysis (415 K, 0.05–20 kPa) detected methanol monomers (~2400  $cm^{-1}$ ) and dimers (~2600  $cm^{-1}$ ) [13], and vibrational modes for methanol clusters (~3370  $cm^{-1}$ ) [51] at high methanol partial pressures (>10 kPa) [16]. Including methanol trimers as a MASI introduces a second-order methanol pressure term in the denominator of the associative dehydration rate law (Eq. (4)), which is able to describe the rate inhibition measured at high methanol partial pressures (Fig. 1, solid line) [16].

$$r_A = \frac{k_{DME,A}K_D P_{CH_3OH}}{1 + K_D P_{CH_3OH} + K_I K_D P_{CH_3OH}^2} \quad (4)$$

In Eq. (4),  $K_I$  is the equilibrium constant for forming a methanol trimer from a gaseous methanol and adsorbed protonated dimer. Before using Eq. (4) to describe methanol dehydration rates on CHA zeolites, we first examine and discard other mechanistic assumptions that would also predict high-pressure kinetic inhibition, by considering other plausible intermediates and rate laws

derived from the dissociative mechanism that do not consider surface methoxy as a MASI, since such species are not detected by *in situ* IR spectra of CHA zeolites (Si/Al = 15) containing isolated  $H^+$  sites [16].

An alternate rate law can be derived for the dissociative mechanism, assuming methanol monomer dehydration to form methoxy intermediates is the kinetically relevant step, and that  $H^+$  sites, methanol monomers, and protonated dimers are the MASI ( $r_{D1}$ ; derivation in Section S.13.1 of the Supp. Info.):

$$r_{D1} = \frac{k_{Me}K_M P_{CH_3OH}}{1 + K_M P_{CH_3OH} + K_M K_D P_{CH_3OH}^2} \quad (5)$$

In Eq. (5),  $k_{Me}$  is the methoxy formation rate constant, and  $K_M$  is the equilibrium constant for forming a methanol monomer from a gaseous methanol and a vacant  $H^+$  site. This expression predicts inhibition at high methanol partial pressures because protonated dimers are spectator species in the dissociative mechanism (Scheme 1). This rate expression would require vacant  $H^+$  sites to be a MASI, however, which is inconsistent with *in situ* IR spectra that show complete perturbation of bridging OH stretching vibrations (~3608  $cm^{-1}$ ) by adsorbates at low methanol partial pressures corresponding to the first-order kinetic regime (<1 kPa  $CH_3OH$ , 415 K) [16]. The removal of vacant  $H^+$  sites as a MASI causes Eq. (5) to predict between zero-order and negative-order dependences on methanol pressure, resulting in a rate law (Eq. (6)) that does not describe the first-order dependence of methanol dehydration rates at low pressures (Fig. 1, dotted line):

$$r_{D1} = \frac{k_{Me}}{1 + K_D P_{CH_3OH}} \quad (6)$$

Another alternative rate law can be derived from the dissociative mechanism, assuming DME formation is the kinetically relevant step and all preceding steps are quasi-equilibrated, and that methanol monomers and protonated dimers are the MASI, in accordance with *in situ* IR spectra measured on CHA zeolites (Si/Al = 15) containing isolated  $H^+$  sites [16] ( $r_{D2}$ ; derivation in Section S.13.2 in the Supp. Info.):

$$r_{D2} = \frac{k_{DME,D}K_{MMe}K_{Me}P_{CH_3OH}P_{H_2O}^{-1}}{1 + K_D P_{CH_3OH}} \quad (7)$$

In Eq. (7),  $k_{DME,D}$  is the DME formation rate constant for the dissociative mechanism,  $K_{MMe}$  is the equilibrium constant for forming a methoxy-methanol pair from a surface methoxy and gaseous methanol, and  $P_{H_2O}$  is the gas-phase partial pressure of water, which is generated via methanol monomer dehydration to form a surface methoxy. This rate law predicts a first-order kinetic regime at low methanol pressures and a transition to a zero-order kinetic regime at higher pressures, but also predicts rate inhibition caused by hydration of surface methoxy intermediates. Eq. (7) was regressed to methanol dehydration rates (per  $H^+$ , 415 K) measured on CHA zeolites containing isolated  $H^+$  sites, assuming that the gaseous water partial pressure is equal to that of DME formed from reaction (Fig. 1, dashed line). The high-pressure inhibition observed experimentally causes methanol conversion to decrease (Fig. 2a) faster than Eq. (7) would predict, indicating that the product water formed via methanol dehydration is unable to account for the measured inhibition (Fig. 1, dashed line). Moreover, methanol dehydration rates do not depend on space velocity at fixed methanol pressure (per  $H^+$ , 1 kPa  $CH_3OH$ , 5–30% conv.; Fig. 2b), as would be predicted by Eq. (7) because of the inverse dependence of methanol dehydration rates on water pressure (solid line, Fig. 2b; derivation in Section S.12 of Supp. Info.). Methanol dehydration rates (415 K, per  $H^+$ ) were also measured after treating methanol reactants to remove any residual moisture and contaminants (purification procedure in Section S.4, Supp. Info.), and were

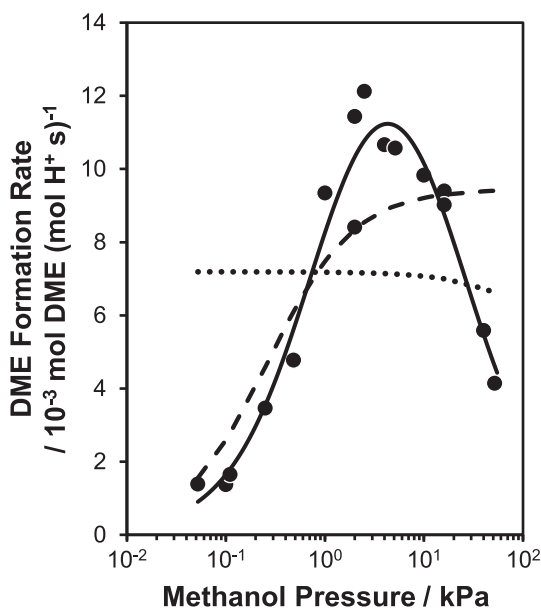
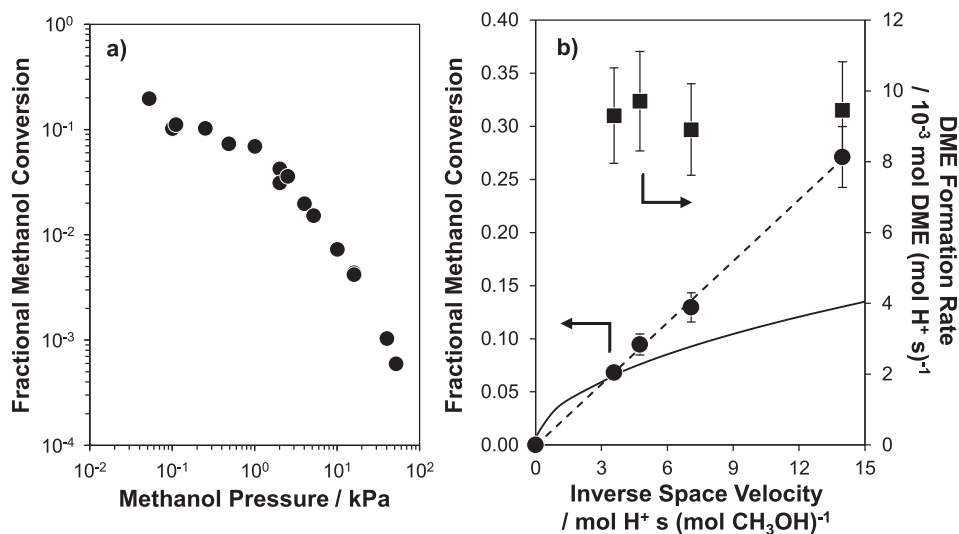


Fig. 1. Least-squares regressions of Eq. (4) (solid line), Eq. (6) (dotted line), and Eq. (7) (dashed line) to experimentally measured methanol dehydration rates (per  $H^+$ , 415 K) on a H-CHA (Si/Al = 15) sample containing predominantly isolated  $H^+$  sites.



**Fig. 2.** (a) Fractional methanol conversion (415 K) on a H-CHA (Si/Al = 15) sample with isolated  $H^+$  sites as a function of methanol pressure, and (b) fractional methanol conversion (circles) and DME formation rates (per  $H^+$ , 415 K; squares) along with the predicted dependence from Eq. (7) (solid line, derivation in Section S.12 of Supp. Info.) as a function of inverse space velocity.

identical to those measured using unpurified methanol (Fig. S.9, Supp. Info.). Thus, any adventitious water present in the reactant methanol feed, or generated *in situ* as a reaction product, is not responsible for the observed inhibition at high methanol pressures.

### 3.2. DFT assessments of prevalent methanol dehydration reaction pathways

Prior to interpreting the mechanistic origin of high-pressure inhibition of methanol dehydration rates, we first use DFT to predict the free energy landscapes (Fig. 3) of both the associative and dissociative mechanism at isolated  $H^+$  sites in CHA (1 bar, 415 K). For the associative mechanism, DME formation from a protonated dimer intermediate is the kinetically relevant (i.e., rate-determining) step, and DFT estimates a zero-order free energy barrier ( $\Delta G_{\text{zero}} = \Delta G_{\ddagger} - \Delta G_{\text{dimer}}$ ) of  $137 \text{ kJ mol}^{-1}$  and first-order free energy barrier ( $\Delta G_{\text{first}} = \Delta G_{\ddagger} - \Delta G_{\text{monomer}} - \Delta G_{\text{CH}_3\text{OH},g}$ ) of  $123 \text{ kJ mol}^{-1}$  (Fig. 3). For the dissociative mechanism, the first step methylates the zeolite surface with an intrinsic and overall barrier of  $135 \text{ kJ mol}^{-1}$ , while the second step involves methylating methanol to form DME with an intrinsic barrier of  $77 \text{ kJ mol}^{-1}$  and

an overall barrier of  $130 \text{ kJ mol}^{-1}$  (Fig. 3). Either of these steps could be kinetically relevant should DME form via the dissociative mechanism. Therefore, the kinetic fates of surface methoxy intermediates were determined by calculating ratio of the reverse rate of the first step ( $r_{-D1}$ ) to the forward rate of the second step ( $r_{D2}$ ) as a function of conversion (details in Section S.3 in Supp. Info.). The forward rate of the second step is  $>10\times$  faster than the reverse rate of the first step below 30% conversion, corresponding to the highest value tested in this work (Fig. S.7, Supp. Info.), and thus the first step is kinetically relevant at these conditions.

The reaction coordinate diagram in Fig. 3 was constructed after carefully examining each intermediate and transition state structure to identify their most stable configurations, using systematic reorientations of initially converged structures to more comprehensively probe the configurational space accessible within zeolite voids [48]. The first step of the dissociative mechanism involves surface methylation transition states that are stabilized by 8-MR structures, in which H atoms of hydroxyl groups form H-bonds to lattice O atoms (Fig. 4a). Surface methylation transition states preferentially interact with O3 of the conjugate base and form two H-bonds to O atoms in the 8-MR, in which O3 is located

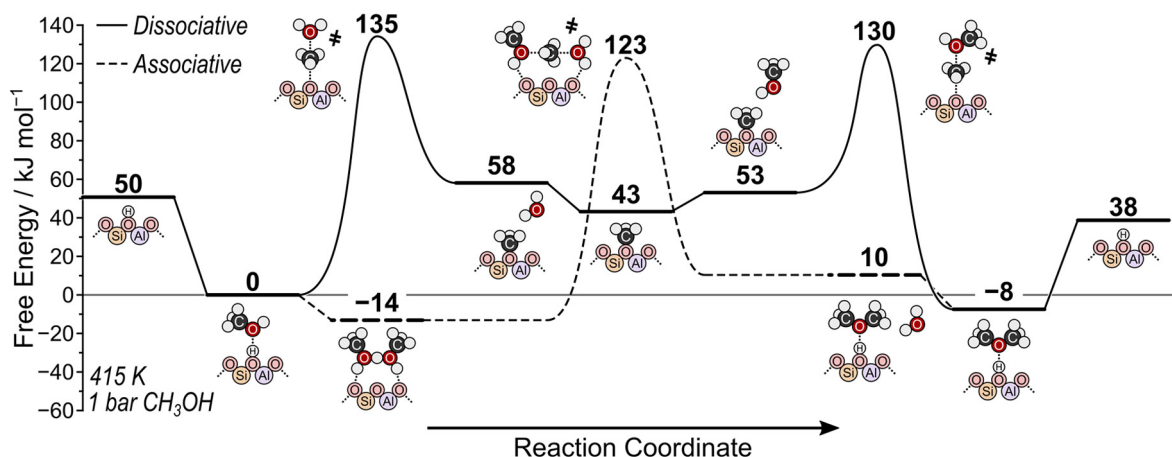


**Fig. 3.** Reaction coordinate diagram showing DFT-calculated free energies ( $\Delta G$ ;  $\text{kJ mol}^{-1}$ ) of intermediates and DFT transition states involved in methanol dehydration on isolated  $H^+$  sites in CHA at 415 K and 1 bar of  $\text{CH}_3\text{OH}$ .

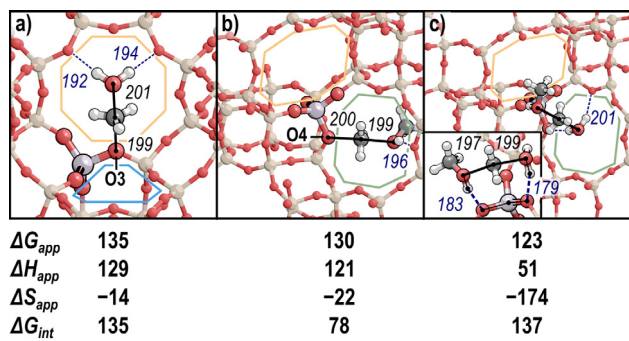


**Fig. 4.** The most favorable transition state found in CHA for (a) surface methylation (the first step of the dissociative mechanism), (b) methanol methylation (the second step of the dissociative mechanism), and (c) associative dimethyl ether formation. The framework O atom with which the methyl group interacts in (a) and (b) is labeled. Incipient bonds (black) and H-bonds (navy) are labeled in pm. Apparent ( $\Delta G_{app}$ ) and intrinsic free energy ( $\Delta G_{int}$ ) and apparent enthalpy ( $\Delta H_{app}$ ) barriers in  $\text{kJ mol}^{-1}$ , and apparent entropies ( $\Delta S_{app}$ ) in  $\text{J mol}^{-1} \text{K}^{-1}$ , are shown relative to an adsorbed methanol. The 8-MR (orange, green) and 6-MR (light blue) adjacent to each transition state are highlighted.

(192 and 194 pm, Fig. 4a). The most favorable surface methylation transition states at O4 and O2, which are also in 8-MR, are 13 and 18  $\text{kJ mol}^{-1}$  higher in energy, respectively, indicating the strong preference for the transition state geometry at O3 for surface methylation (Fig. S.2 in the Supp. Info.). The transition state at O1 is 38  $\text{kJ mol}^{-1}$  higher in energy than that at O3, as this transition state is not solvated by surrounding framework atoms (Fig. S.2 in the Supp. Info.), because it is instead located in the larger CHA cage void, which confers weaker dispersive stabilization.

The second step of the dissociative mechanism, in which another methanol accepts the surface methyl group, also occurs most easily in the 8-MR; however, this transition state forms preferentially at O4 of the conjugate base rather than at O3 (Fig. 4b). The methanol that accepts the surface methyl group forms one H-bond to another O atom in the 8-MR that contains O4 of the active site. The reacting oxygenate species ( $\text{CH}_3\text{OH}$ ) contains only one polar O—H bond instead of two ( $\text{H}_2\text{O}$ ), resulting in less H-bonding capacity in this transition state than in the other two possible transition states that occur during methanol dehydration (Fig. 4). Moreover, this H-bond is longer (196 pm; Fig. 4b) and weaker than the H-bonds formed in surface methylation (192 and 194 pm; Fig. 4a) and associative DME formation (179 and 201 pm; Fig. 4c) transition states.

The associative transition state (Fig. 4c) is stabilized by 8-MR structures similarly to surface methylation transition states (Fig. 4a). The water leaving group in this transition state forms two H-bonds to framework O atoms in the 8-MR, one of which is O4 of the conjugate base and stabilizes partial charges of the transition state structure. Furthermore, the methanol that accepts the methyl group forms another H-bond to O3 of the conjugate base, again stabilizing the transition state and allowing for rapid surface protonation after DME is formed. These concerted H-bonding motifs form a ring of interactions as the methyl group is transferred from one oxygenate to another (Fig. 4c, inset), allowing for more effective charge distribution than is possible in either of the dissociative transition states. Moreover, H-bonding in the associative transition state occurs predominantly with O atoms of the conjugate base, which harbor more negative partial charge, resulting in shorter (181 pm on average in Fig. 4c; 193 and 196 pm in Fig. 4) and stronger stabilizing interactions between reacting species and the zeolite surface.

Maximum rate analysis was then used to predict rates of competing reaction pathways using these DFT-predicted free energy

barriers, which are taken together with statistical mechanics formalisms (see Section S.1 of the Supp. Info. for relevant formulas) to calculate rate ( $k_i$ ) and equilibrium constants ( $K_i$ ), as described in previous work [48,52]. The overall rate of a reaction pathway is taken as the rate of the slowest elementary step, identified from rates calculated by separately considering each elementary step to be the sole rate-limiting step. The fastest overall rates among different competing reaction pathways are used to identify prevailing reaction routes. Although the associative route occurs with an overall barrier 12  $\text{kJ mol}^{-1}$  lower than that of the dissociative route at 415 K (123  $\text{kJ mol}^{-1}$  overall; Fig. 3), the resulting larger rate constant does not account for pressure effects on rates, requiring maximum rate analysis to assess competing dehydration pathways.

The results of maximum rate analysis at 415 K and 0.1% conversion are shown in Fig. 5, with rates of the associative pathway and of the first and second steps of the dissociative pathway shown as a function of methanol pressure. The second step of the dissociative pathway occurs at faster rates than the associative mechanism at all pressures considered here (0.01–100 kPa) (Fig. 5), consistent with analysis of the reversibility of the first step that indicates it is the sole kinetically relevant step of the dissociative mechanism (Section S.3, Supp. Info.). The dissociative pathway dominates at pressures below 4 kPa at 415 K, which reflects the relative pressure dependences of rates for the associative and dissociative routes:

$$\frac{r_{D1}}{r_A} = \frac{k_{D1}}{k_A K_D P_{\text{CH}_3\text{OH}}} \quad (8)$$

This equation indicates that the dissociative route will dominate at sufficiently low methanol pressures, and that the prevailing reaction mechanism will shift to the associative route at higher pressures. Rates estimated by DFT predict this transition occurs at 4, 10, 23, and 63 kPa at 415, 433, 450, and 473 K, respectively (Fig. S.6b). This shift reflects entropic and enthalpic preferences for these routes, in which the adsorption of a second methanol in the associative route confers enthalpic gains but concomitant entropic losses that preferentially benefit the dissociative mechanism at high temperatures and low pressures. This is consistent

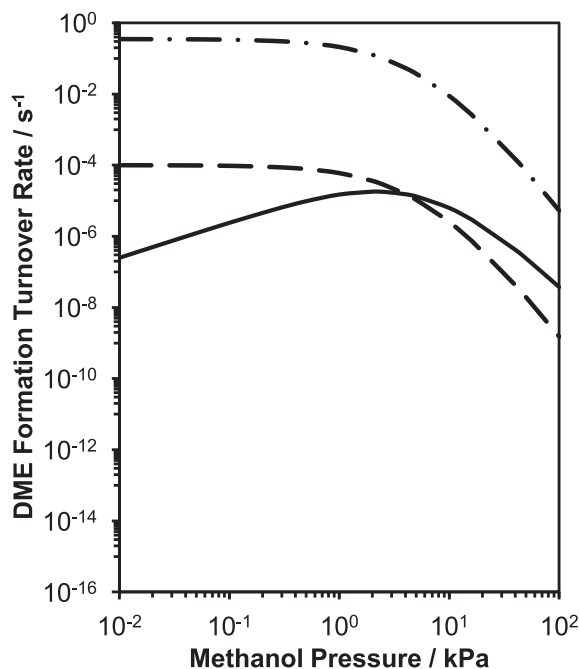


**Fig. 5.** DFT-predicted rates (415 K) for kinetically-relevant methoxy (dashed line) and DME (dashed-dotted line) formation steps of the dissociative mechanism, and for the associative mechanism (solid line) at 0.1%  $\text{CH}_3\text{OH}$  conversion.



with prior work on MFI zeolites [12,13,15] and POM catalysts [10], which indicate similar behavior for these mechanisms with different kinetic conditions.

### 3.3. Generality of high-pressure kinetic inhibition on small-pore zeolites and its dependence on temperature

Taken together, the experimental data in Section 3.1 provide strong evidence that methanol dehydration proceeds via the associative dehydration mechanism at isolated  $H^+$  sites in CHA zeolites. These findings are consistent with previous investigations of methanol dehydration on microporous (medium-pore, large-pore) and mesoporous solid Brønsted acid catalysts that have compared both dehydration mechanisms under conditions where sites are covered by methanol monomers and dimers (433 K, 0.2–16 kPa  $CH_3OH$ ) [10,12,13,53,54]. In Section 3.2, the DFT-calculated free energy barriers (415 K) on isolated  $H^+$  sites in CHA zeolites in both the first-order and zero-order regime for the associative mechanism show closer agreement with values measured experimentally (Table 1). Moreover, maximum rate analysis indicates that the associative mechanism prevails at sufficiently high methanol pressures (>4 kPa) in CHA containing only isolated  $H^+$  sites.

We next experimentally probed whether high-pressure inhibition is a general feature of small-pore microporous acids, given that such high-pressure inhibition of methanol dehydration rates was also observed in our prior studies of CHA zeolites with different fractions of paired  $H^+$  sites [16]. Methanol dehydration rates (415 K, per  $H^+$ ) were measured as a function of methanol pressure on other small-pore zeolite frameworks including AEI, LEV, and LTA, and the data are shown in Fig. 6. Methanol dehydration rates on all small-pore zeolites show a first-order kinetic regime at low methanol pressures, before reaching a maximum and then decreasing with increasing methanol pressure. These data suggest that small-pore zeolite framework topologies, in general, assist in stabilizing inhibitory methanol species at sufficiently high methanol partial pressures.

CHA zeolites (Si/Al = 15) containing predominantly isolated  $H^+$  sites were chosen as representative samples to further study the mechanistic origin of the high-pressure inhibition of methanol dehydration rates in small-pore zeolites. High-pressure inhibition becomes attenuated in CHA containing only isolated  $H^+$  sites (Fig. 7a), and in CHA containing paired  $H^+$  sites (Fig. S.15, Supp. Info.), with increasing reaction temperature (398–473 K). This behavior is inconsistent with that expected if inhibition were to reflect intracrystalline transport restrictions of larger DME products, which would cause inhibition to become more severe with increasing temperature. Light olefins (e.g., ethene and propene) were observed in the reactor effluent at low methanol partial pressures at temperatures >433 K, and decreased in concentration with increasing methanol partial pressures, consistent with previous reports of methanol-to-olefins in H-MFI (623 K) [4]. First-order rate constants (per  $H^+$ ), extracted from linear regression of Eq. (3) to the data in Fig. 7a, initially increase exponentially with temperature (398–415 K), but begin to deviate from this exponential

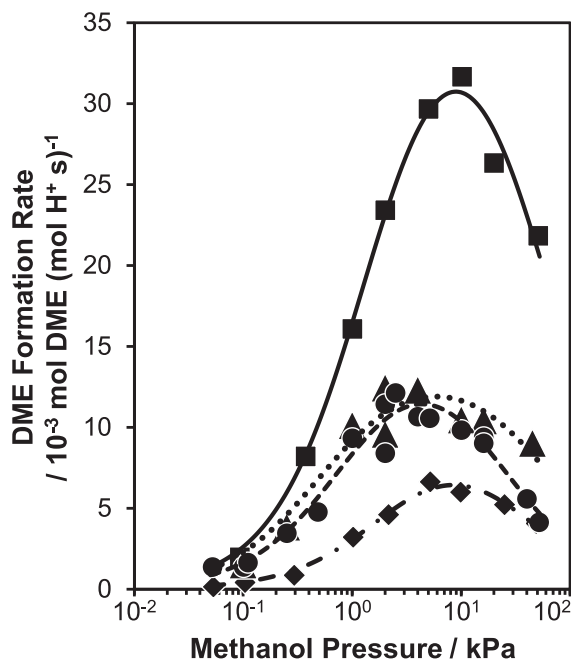


Fig. 6. Measured (data points) and regressed (lines; Eq. (3)) DME formation rates (415 K, per  $H^+$ ) on representative AEI (squares; solid), CHA (circles; dashed), LEV (triangles; dotted), and LTA (diamonds; dash-dot) zeolites as a function of methanol pressure.

dependence at elevated temperatures (433–473 K; Fig. 7b), in part reflecting scavenging of  $C_1$  intermediates and DME products to produce olefins under first-order methanol dehydration conditions (<1 kPa). In contrast, zero-order rate constants (per  $H^+$ ) increase exponentially with temperature in the range studied (398–473 K), suggesting that any olefin formation does not significantly influence DME formation rates at high methanol pressures (>10 kPa  $CH_3OH$ ) [4]. These results suggest that methanol dehydration rates are not inhibited by intracrystalline transport of DME products and instead may reflect inhibition by absorption of excess methanol molecules as proposed previously [17], as would be expected from the decrease in methanol coverage with increasing temperature at fixed methanol pressure.

The adsorbed methanol structures on CHA zeolites containing isolated  $H^+$  sites at varying temperatures (343–473 K) were assessed from *in situ* IR spectra measured at 10 kPa  $CH_3OH$ , which coincides with the onset of inhibition in CHA zeolites (Fig. 1).  $CH_3OH$  cluster ( $\sim 3370\text{ cm}^{-1}$ ) [51] formation is a strong function of temperature (Fig. 8), evident by IR peaks that decrease in intensity at faster rates than those for protonated methanol dimers ( $2620\text{ cm}^{-1}$ ; Fig. 8, inset) [13], suggesting that methanol adsorbs in clusters (e.g., trimers, tetramers) [51] more weakly than in protonated dimer structures. These findings are consistent with the adsorption of excess methanol at protonated methanol dimers, and with the attenuated inhibition of methanol dehydration rates at higher reaction temperatures (398–473 K; Fig. 7).

### 3.4. Adsorbed methanol structures as a function of coverage assessed from *in situ* IR spectra, equilibrium adsorption isotherms, and DFT-calculated free energies

Methanol adsorption isotherms (293 K; full isotherm shown in Fig. S.16 of Supp. Info.), normalized to the number of  $H^+$  sites, were used to determine methanol coverage ( $\theta_{CH_3OH}$ , per  $H^+$  site; Fig. 9a) on isolated  $H^+$  sites in CHA zeolites as a function of methanol relative pressure ( $P/P_{sat}$ ;  $P_{sat}$  is the saturated methanol vapor

Table 1

Measured and calculated first-order and zero-order free energy barriers ( $\Delta G$ ;  $\text{kJ mol}^{-1}$ ) at 415 K for the associative and dissociative dehydration mechanisms at isolated  $H^+$  sites in CHA zeolites.

	$\Delta G_{\text{first}}$ ( $\text{kJ mol}^{-1}$ )	$\Delta G_{\text{zero}}$ ( $\text{kJ mol}^{-1}$ )
Measured <sup>a</sup>	100	117
Associative <sup>b</sup>	123	137
Dissociative <sup>b</sup>	135	77

<sup>a</sup> Calculated from rate data measured between 383 and 415 K.

<sup>b</sup> Calculated from DFT (PBE-D3BJ, PAW).

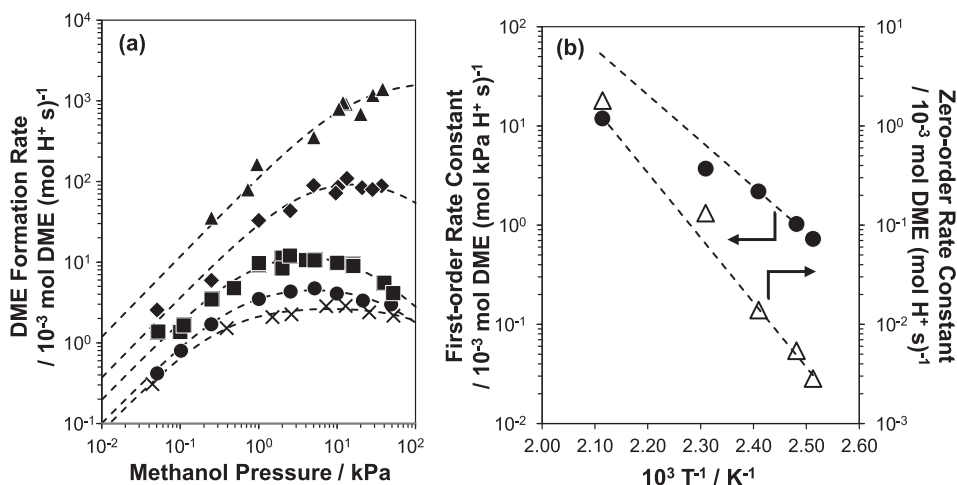


**Fig. 7.** (a) DME formation rates (per  $\text{H}^+$ ) measured at 398 K (crosses), 403 K (circles), 415 K (squares), 433 K (diamonds), and 473 K (triangles) on CHA (Si/Al = 15) containing isolated  $\text{H}^+$  sites. Dashed lines are linear regressions to Eq. (4). (b) First-order (closed circles) and zero-order (open triangles) rate constants (per  $\text{H}^+$ ) measured as a function of temperature (398–473 K) on CHA (Si/Al = 15) containing isolated  $\text{H}^+$  sites. Dashed lines are exponential fits to the data between 398 and 415 K.

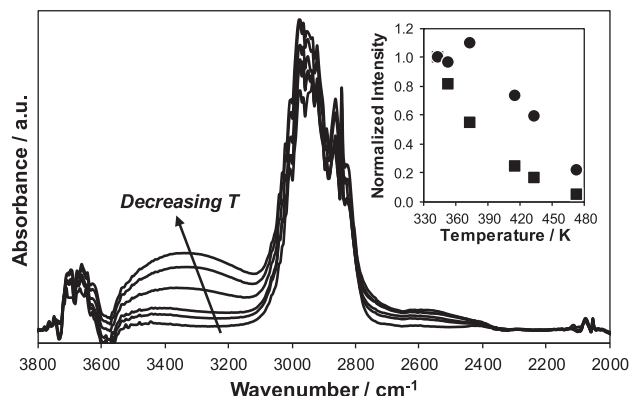


**Fig. 8.** IR spectra of H-CHA (Si/Al = 15, isolated Al) at 10 kPa  $\text{CH}_3\text{OH}$  measured at 343 K, 353 K, 373 K, 415 K, 433 K, and 473 K. Inset shows the intensity of the IR peaks for methanol clusters ( $\sim 3370 \text{ cm}^{-1}$ ; squares) and protonated methanol dimers ( $\sim 2620 \text{ cm}^{-1}$ ; circles) as a function of temperature, normalized to the peak intensity at 343 K.

pressure). Differential changes in methanol coverage ( $\alpha$ ) were calculated from the derivative of the methanol coverage isotherm (Fig. 9a) with respect to the logarithmic change in reduced pressure, according to the following equation:

$$\alpha = \frac{\partial \theta_{\text{CH}_3\text{OH}}}{\partial \left( \ln \left( \frac{P}{P_{\text{sat}}} \right) \right)} \quad (9)$$

Values of  $\alpha$  are plotted as the secondary abscissa in Fig. 9a, and used to assess the rate of change of methanol coverage as a function of relative pressure in order to identify transitions in methanol chemisorption regimes, as typically done to identify transitions in physisorption regimes of non-interacting adsorbates (e.g.,  $\text{N}_2$ , Ar) caused by the filling of pores of different characteristic size [55,56].

At low methanol coverages ( $< 1 \text{ CH}_3\text{OH}$  per  $\text{H}^+$  site), adsorption is characterized by an initial maximum ( $\sim 0.6 \text{ CH}_3\text{OH}$  per  $\text{H}^+$ ) in the differential methanol coverage isotherm, followed by a local minimum at  $\sim 1 \text{ CH}_3\text{OH}$  (per  $\text{H}^+$ ) (Fig. 9a). This adsorption behavior is characteristic of pore filling in the case of non-interacting adsorbates (e.g., Ar,  $\text{N}_2$ ) within microporous voids [57], but in the case of

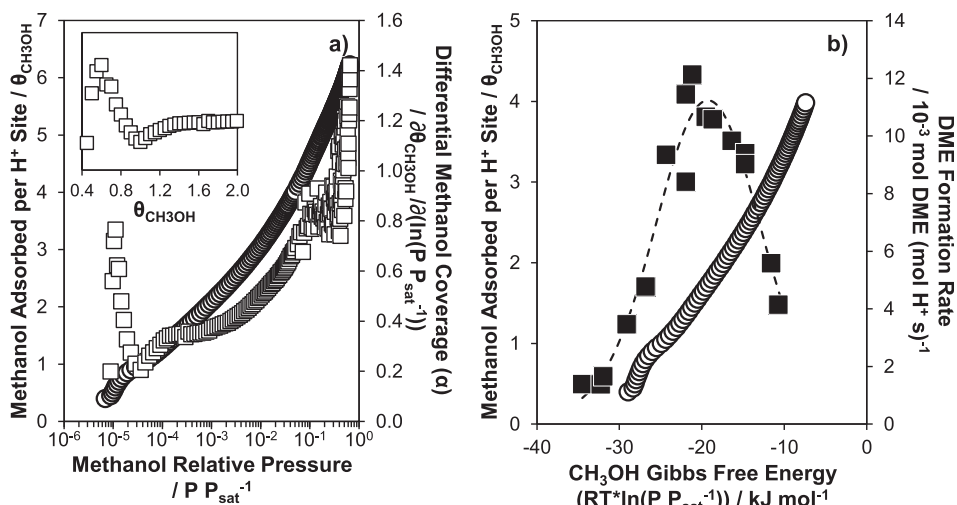


**Fig. 9.** (a) Methanol coverage ( $\text{CH}_3\text{OH}$  per  $\text{H}^+$  site; circles) and the differential methanol coverage (Eq. (9); squares) as a function of methanol relative pressure on H-CHA containing only isolated  $\text{H}^+$  sites at 293 K. The inset shows a magnified version of the differential methanol coverage versus methanol coverage at low methanol relative pressures ( $P/P_{\text{sat}} < 10^{-3}$ ). (b) DME formation rate (415 K, per  $\text{H}^+$ ; squares) and methanol coverage (293 K, per  $\text{H}^+$ ; circles) measured on H-CHA containing only isolated  $\text{H}^+$  sites as a function of the gas-phase methanol Gibbs free energy (Eq. (10)). Dashed line is a fit of Eq. (4) to experimental DME formation rates (415 K, per  $\text{H}^+$ ).

methanol reflects the selective adsorption at  $H^+$  sites to form methanol monomers at coverages  $<1$   $CH_3OH$  (per  $H^+$ ). Continued adsorption of methanol results in a second maximum and subsequent local minimum in the differential isotherm at  $\sim 1.7$   $CH_3OH$  (per  $H^+$ ), which reflects the adsorption of a second methanol to form protonated dimers. This local minimum is then followed by the continuous adsorption of additional methanol with increasing methanol pressure until saturation of the CHA pore volume is achieved at a value corresponding to  $>6$   $CH_3OH$  ( $\sim 0.20$   $cm^3$   $g^{-1}$   $CH_3OH$  adsorbed at STP).

Methanol coverages (per  $H^+$ ) at the temperatures of catalysis cannot be measured directly, and were instead estimated from equilibrium methanol adsorption data measured at 293 K by first transforming methanol relative pressure into an equivalent methanol Gibbs free energy ( $\Delta G_{CH_3OH}$ ) according to the following equation (derivation in Section S.16 of the Supp. Info.):

$$\Delta G_{CH_3OH} = RT \ln \left( \frac{P}{P_{sat}} \right) \quad (10)$$

where  $R$  is the ideal gas constant ( $8.314$   $J$   $mol^{-1}$   $K^{-1}$ ),  $T$  is the temperature (K),  $P$  is the absolute methanol pressure, and  $P_{sat}$  is the methanol vapor pressure (at  $T$ ). The value of  $\Delta G_{CH_3OH}$  reflects equilibrium between gaseous and liquid-like intrazeolitic methanol species as a function of methanol pressure and temperature. Methanol coverages are plotted as a function of the  $\Delta G_{CH_3OH}$  (293 K, Fig. 9b), calculated from adsorption isotherm data (Fig. 9a) and Eq. (10). DME formation rates (415 K, per  $H^+$ ) are also plotted as a function of  $\Delta G_{CH_3OH}$  (Fig. 9b), after normalizing the methanol partial pressures at which rates were measured (0.05–50 kPa) by the vapor pressure of methanol at 415 K according to Eq. (10). DME formation rates show a first-order dependence on  $\Delta G_{CH_3OH}$  values corresponding to methanol coverages of  $\sim 1$   $CH_3OH$  (per  $H^+$ ), and begin to transition towards a zero-order kinetic regime for  $\Delta G_{CH_3OH}$  values corresponding to methanol coverages approaching 2  $CH_3OH$  (per  $H^+$ ). The onset of inhibition coincides with  $\Delta G_{CH_3OH}$  values of  $\sim -19.4$   $kJ$   $mol^{-1}$  (Fig. 9b) that correspond to methanol coverages exceeding  $\sim 2$   $CH_3OH$  (per  $H^+$ ). These results further corroborate the interpretation that methanol dehydration rates (415 K) in CHA zeolites become inhibited upon adsorption of methanol beyond protonated dimer structures, and that such inhibition becomes more severe as additional methanol adsorbs within microporous voids at higher methanol partial pressures.

The structures of adsorbed methanol were also monitored by *in situ* IR spectra (293 K) collected upon dosing methanol in fractional quantities ( $\sim 0.05$   $CH_3OH$  per  $H^+$  per dose), as shown in Fig. 10. Only bare  $H^+$  sites ( $\sim 3605$   $cm^{-1}$ ) and methanol monomers ( $\sim 2380$   $cm^{-1}$ ) are detected at low coverages of  $<0.3$   $CH_3OH$  (per  $H^+$ ). Protonated methanol dimers ( $\sim 2600$   $cm^{-1}$ ) begin to appear beyond a coverage of  $\sim 0.3$   $CH_3OH$  (per  $H^+$ ), and increase in intensity to saturation at  $\sim 2.3$   $CH_3OH$  (per  $H^+$ ). At methanol coverages  $>0.7$   $CH_3OH$  (per  $H^+$ ), peaks characteristic of methanol clusters ( $\sim 3300$   $cm^{-1}$ ) are observed and increase in intensity with methanol coverage up to 3  $CH_3OH$  (per  $H^+$ ), even after saturation of monomer and dimer features occurs. These data provide spectroscopic evidence for the formation of methanol clusters ( $>2$   $CH_3OH$  per  $H^+$  site) at gas-phase methanol free energies that correspond to the onset of inhibition of methanol dehydration rates (415 K, per  $H^+$ ) in CHA zeolites.

Adsorption free energy values are calculated using DFT to estimate equilibrium constants, and thus most stable methanol cluster size (per  $H^+$ ) at an isolated  $H^+$  site in CHA as a function of methanol partial pressure and temperature. Free energies of adsorption of methanol clusters ranging in size from 0 to 12 methanol molecules were computed to estimate the most stable species at an isolated  $H^+$  site in CHA over a wide range of methanol pressures

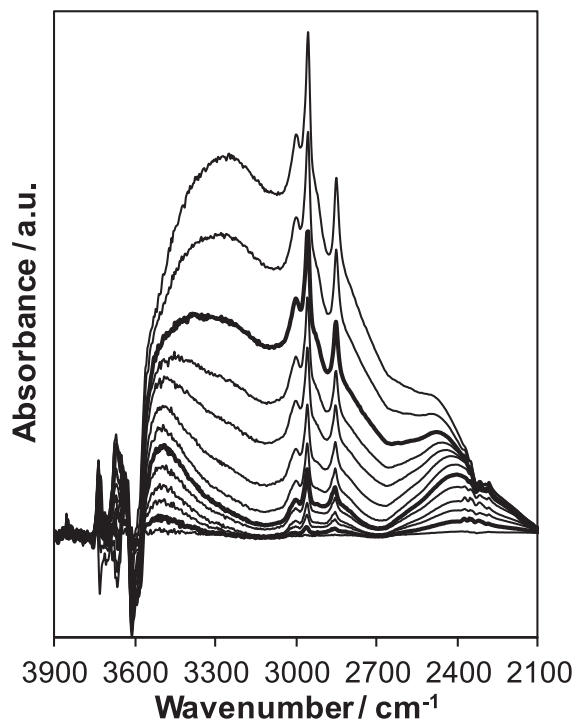


Fig. 10. IR spectra measured at 293 K on H-CHA (Si/Al = 15) with isolated  $H^+$  sites as a function of methanol dosing (0.01–3  $CH_3OH/H^+$ ).

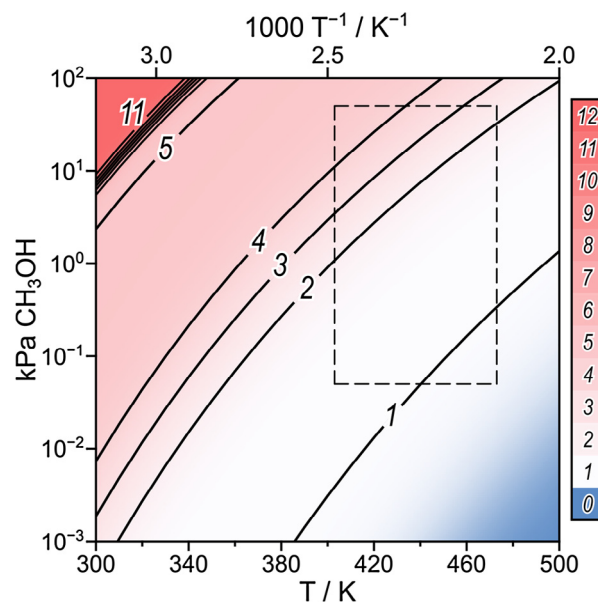


Fig. 11. Phase diagram predicting the average methanol cluster size at isolated  $H^+$  sites in CHA, denoted by the phase boundary lines in the figure and the colored legend to the right of the figure. Equilibrium constants for adsorption were predicted by free energies from DFT at 415 K and 1 bar  $CH_3OH$ . The area enclosed by dashed lines correspond to the range of kinetic conditions studied for methanol dehydration in this work (403–473 K, 0.05–50 kPa  $CH_3OH$ ).

( $10^{-3}$ – $10^2$  kPa  $CH_3OH$ ) and temperatures (300–500 K), as shown in Fig. 11. Methanol clusters deprotonate  $H^+$  sites and form extended cationic networks with each other, in which methanol molecules link two O atoms of the  $AlO_4^-$  conjugate base through a series of H-bonds (additional details and data in Section S.15, Supp. Info.). At low temperatures and high methanol pressures ( $<350$  K,  $>50$  kPa  $CH_3OH$ ), the most stable methanol cluster rapidly

shifts from a pentamer to a dodecamer (12 CH<sub>3</sub>OH\*); Fig. 11). The predicted formation of these dodecamers is analogous to capillary condensation, when enthalpic stabilization conferred by adsorption of large quantities of methanol (or another adsorbate) leads to rapid filling of zeolite pores. Notably, these dodecamers have approximately the same density (12 CH<sub>3</sub>OH\* per unit cell) as the methanol-saturated CHA samples measured experimentally (Fig. 9a). These CHA samples (Si/Al = 15) contain 2.25 H<sup>+</sup> per unit cell, while the DFT model (Si/Al = 35) contains 1 H<sup>+</sup> per unit cell; therefore, these DFT calculations reflect the pore-filling behavior observed experimentally.

The area enclosed by the dashed lines in Fig. 11 corresponds to the reaction conditions studied here, and methanol monomers and dimers dominate the surface of CHA at pressures below 3 kPa CH<sub>3</sub>OH at 415 K. At high temperatures (>450 K) and low methanol pressures (<10<sup>-2</sup> kPa CH<sub>3</sub>OH), empty H<sup>+</sup> sites are predicted to be the most favorable conformation because entropic considerations favor desorption into the gas-phase, assuming adsorbed methanol molecules do not react (Fig. 11). Methanol trimers become the most prevalent cluster size at higher methanol pressures (3–13 kPa CH<sub>3</sub>OH) at 415 K, which coincides with the onset of inhibition in experimentally measured DME formation rates (415 K, Fig. 1). DFT predicts that isolated H<sup>+</sup> sites in CHA are covered with a mixture of methanol tetramers and pentamers (~4.5 CH<sub>3</sub>OH per H<sup>+</sup>) at 50 kPa, the highest partial pressure where DME formation rates were measured. These results are consistent with experimentally measured methanol adsorption isotherms that indicate high-pressure kinetic inhibition occurs when coverages exceed two CH<sub>3</sub>OH (per H<sup>+</sup>) at 415 K (Fig. 9). The inhibition of methanol dehydration rates becomes attenuated at elevated temperatures in CHA zeolites (Fig. 7), consistent with DFT-predicted methanol coverages that decrease systematically with increasing temperature (>433 K). From examining the DFT-predicted coverages at the 50 kPa isobar, methanol coverages change from a mixture of tetramers and pentamers at 415 K to a mixture of dimers and trimers at 473 K (Fig. 11). These observations are consistent with the disappearance of methanol clusters at elevated temperatures (>433 K, Fig. 8) and with attenuated high-pressure inhibition of methanol dehydration rates at elevated temperatures (>433 K, Fig. 7).

Methanol clusters around Brønsted acid sites form extended networks with each other, in which methanol molecules link two O atoms of the acid site through a series of H-bonds (Fig. 12). The methanol monomer prefers to adsorb to O4 in CHA and interact with another O atom in the associated 8-MR (Fig. 12a). Monomers interact with only a proton bound to one O atom of the Brønsted acid site; however, as more methanol adsorbs, the site deprotonates to form protonated clusters that interact with multiple O atoms of the conjugate base. This multisite interaction has been shown in previous theoretical studies of methanol dehydration on MFI and on POM clusters [10,53,54,58]. Complexes comprised of 2–5 CH<sub>3</sub>OH prefer to interact with O3 and O4 of CHA concurrently (Fig. 12b–e). As clusters expand, the distance over which they can interact increases, allowing for clusters of >5 CH<sub>3</sub>OH to interact with O4 and O1 through both 8-MR adjacent to the Al T-site (Fig. S.18, Supp. Info).

This set of kinetic, spectroscopic, and theoretical data indicates that the low-temperature (415 K) dehydration of methanol to DME proceeds via the associative dehydration mechanism in CHA zeolites containing predominantly isolated H<sup>+</sup> sites and is inhibited by the formation of methanol clusters at high methanol partial pressures (>10 kPa). Although formation of these higher-order clusters can be included as separate elementary steps in a more comprehensive reaction mechanism, deriving a rate law to describe high-pressure inhibition becomes convoluted by the inability to distinguish whether a specific methanol cluster is solely responsible for inhibition, or whether parallel DME formation routes from higher-order clusters proceed at different rates via interactions of additional methanol with the relevant precursor and transition states. Perturbation of methanol dehydration turnover rates (per H<sup>+</sup>, 473 K) by the presence of neighboring Na<sup>+</sup> atoms on partially-exchanged POM clusters [59] further suggests that the presence of excess methanol may alter the free energy landscape for DME formation in CHA zeolites. These different possibilities can be described by a generalized rate law accounting for the superposition of parallel DME formation routes at H<sup>+</sup> sites covered with different methanol cluster sizes:

$$r_A = \frac{\sum_{j=2}^k \alpha_j P_{\text{CH}_3\text{OH}}^j}{\sum_{m=1}^n \beta_m P_{\text{CH}_3\text{OH}}^m} \quad (11)$$

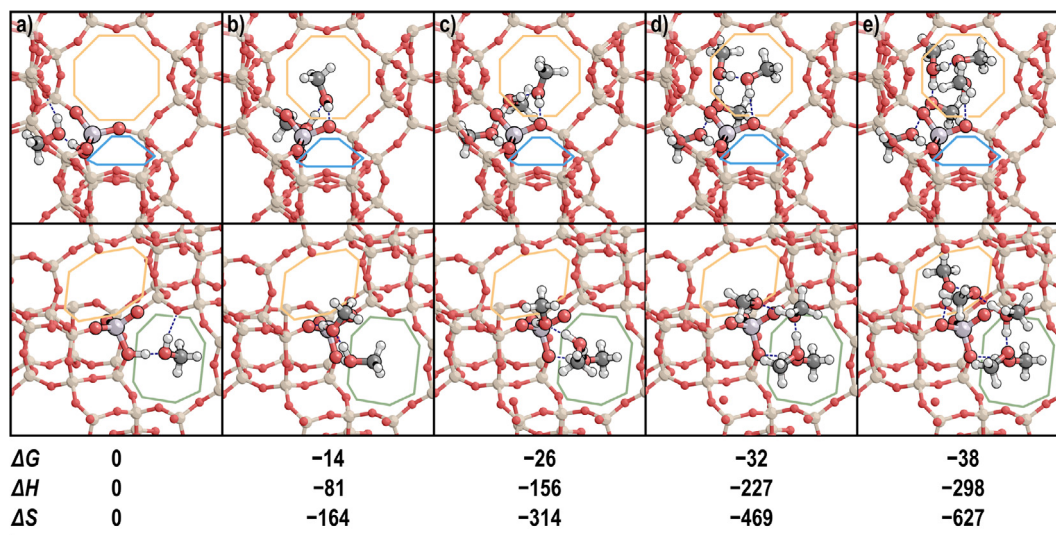


**Fig. 12.** The most stable methanol clusters comprised of (a) a methanol monomer (CH<sub>3</sub>OH\*), (b) a methanol dimer (2 CH<sub>3</sub>OH\*), (c) a methanol trimer (3 CH<sub>3</sub>OH\*), (d) a methanol tetramer (4 CH<sub>3</sub>OH\*), and (e) a methanol pentamer (5 CH<sub>3</sub>OH\*). Free energies ( $\Delta G$ ) and enthalpies ( $\Delta H$ ) in kJ mol<sup>-1</sup>, and entropies ( $\Delta S$ ) in J mol<sup>-1</sup> K<sup>-1</sup>, are shown relative to the methanol monomer at 415 K and 1 bar CH<sub>3</sub>OH. The 8-MR (orange, green) and 6-MR (blue) adjacent to each structure are highlighted. H-bonds are indicated with dashed lines (navy) and are all 170–250 pm.

where,  $j$  represents the number of methanol (i.e., 2 through  $k$  molecules) involved in the transition state,  $\alpha_j$  represents the apparent rate constants for DME formation when  $j$  methanol are involved in the transition state,  $m$  represents the number of methanol (i.e., 1 through  $n$  molecules) in the various MASI species (e.g., monomers, dimers, higher-order clusters), and  $\beta_m$  represents the apparent equilibrium constants to form a methanol cluster containing  $m$  molecules from a gaseous methanol and an adsorbed cluster containing  $m-1$  methanol molecules. While this rate law (Eq. (11)) describes all possible DME formation routes and surface coverages, it does not provide additional mechanistic insight into the nature of high-pressure inhibition in small-pore zeolites. In the following section, we thus use DFT to investigate various DME formation routes via intermediates and transition states at different coverage, pressures, and temperatures in at isolated  $H^+$  sites in CHA zeolites.

### 3.5. DFT-predicted DME formation rates at different methanol coverages

DME formation can occur after desorption of excess methanol to form the kinetically relevant transition state, or in the presence of adsorbed spectating methanol molecules, which can influence the stabilities of the dehydration transition state and its relevant precursor state. Here, we calculate the Gibbs free energy barrier of each methanol dehydration transition state with up to four  $CH_3OH$  co-adsorbed at an isolated  $H^+$  site in CHA. This approach accounts for the potential contributions from parallel DME formation pathways that occur with additional spectating methanol and gives mechanistic insight into the interactions during catalysis from larger clusters of oxygenates in zeolites.

Surface methylation transition states prefer to form H-bonds with spectating  $CH_3OH$  species rather than with framework O atoms (Fig. 13), because the methanol O–H bond is more polar than framework Si–O bonds, enhancing H-bonding between these hydroxyl moieties. Therefore, spectating methanol species prefer to insert themselves where H-bonds between transition states

and framework O atoms are otherwise located in the absence of spectating adsorbates (Fig. 4a). Intrinsic reaction free energy barriers ( $\Delta G_{int}$ ) are essentially unaffected by the insertion of one spectating species into transition states ( $135 \text{ kJ mol}^{-1}$  without spectator to  $134 \text{ kJ mol}^{-1}$  with one spectator), but increase upon insertion of multiple spectating species ( $155$  and  $143 \text{ kJ mol}^{-1}$  for two and three spectating methanol molecules, respectively) as they crowd the transition state and inhibit its formation (Fig. 13). In contrast, apparent barriers ( $\Delta G_{app}$ ) for surface methylation transition states remain similar ( $130$ – $135 \text{ kJ mol}^{-1}$ ), except for that with one spectating methanol ( $121 \text{ kJ mol}^{-1}$ ), as larger methanol clusters become favored at the conditions at which free energies are approximated ( $415 \text{ K}$ ,  $1 \text{ bar}$ ). Despite higher  $\Delta G_{int}$  values with additional spectating molecules,  $\Delta G_{app}$  values remain essentially unchanged because enthalpic stabilization conferred by H-bonding with additional methanol compensates for the entropic losses to form larger clusters. These data indicate that the first step of the dissociative dehydration mechanism occurs with lower standard state ( $1 \text{ bar}$ ) free energy barriers in the presence of a spectating methanol at isolated  $H^+$  sites in CHA ( $415 \text{ K}$ ).

Similarly, the second step of the dissociative route can occur in the presence of spectating methanol (Fig. 14). The intrinsic barriers for this second step decrease in the presence of additional spectating methanol molecules from  $78$  to  $35$ – $36 \text{ kJ mol}^{-1}$  (Fig. 14). The methanol accepting the surface methoxy group forms additional H-bonds to spectating methanol in the most stable transition states identified, because framework Si–O bonds are less polar than hydroxyl O–H bonds of spectating methanol, which favors H-bonding between methanol species during reaction as in the case of surface methylation reactions. The insertion of these co-adsorbed methanol molecules into the transition states also overcomes strain in forming H-bonding networks between the cationic transition state and the zeolite framework. The stronger H-bonds provided by co-adsorbed methanol molecules stabilize dissociative DME formation transition states more than the precursor state,  $CH_3-Z$ , leading to decreases in intrinsic barriers with spectating

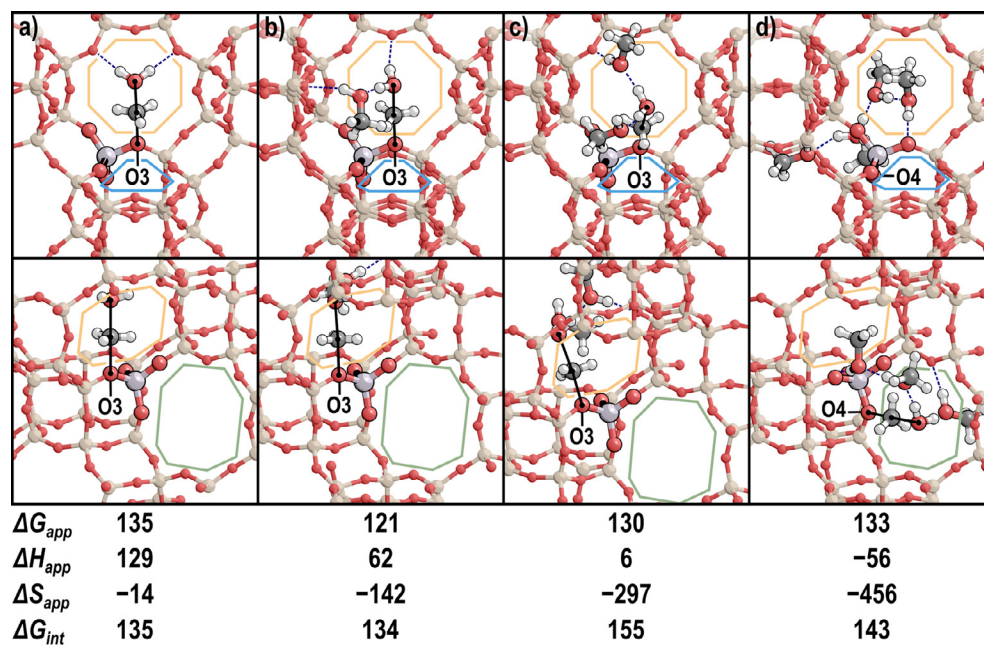


**Fig. 13.** The most favorable surface methylation transition state with (a) zero, (b) one, (c) two, and (d) three spectating  $CH_3OH$  molecules. Incipient and breaking bonds of the transition state are shown with black lines and H-bonds in navy. The O atom with which the methyl group is interacting is labeled. Apparent free energies ( $\Delta G_{app}$ ) and enthalpies ( $\Delta H_{app}$ ) in  $\text{kJ mol}^{-1}$ , and entropies ( $\Delta S_{app}$ ) in  $\text{J mol}^{-1} \text{K}^{-1}$ , are shown relative to an adsorbed methanol. Intrinsic free energy barriers ( $\Delta G_{int}$ ) are shown in  $\text{kJ mol}^{-1}$ . The 8-MR (orange, green) and 6-MR (blue) adjacent to each transition state are highlighted.

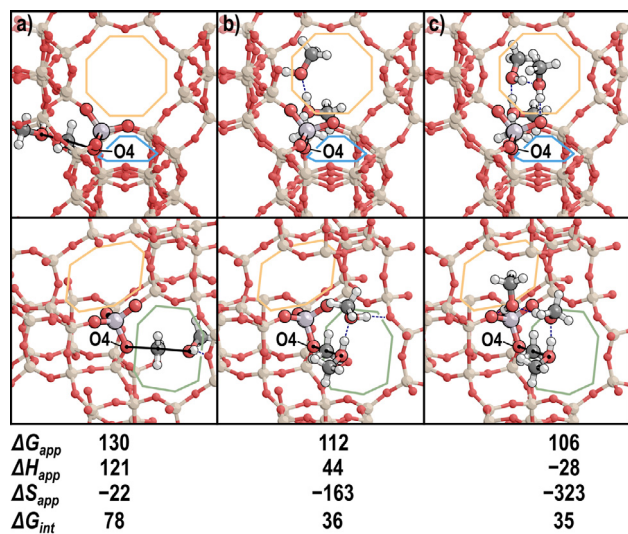


**Fig. 14.** The most favorable transition states for the second step of the dissociative route with (a) zero, (b) one and (c) two spectating  $\text{CH}_3\text{OH}$  molecules. Incipient and breaking bonds of the transition state are shown with black lines and H-bonds in navy. The O atom with which the methyl group is interacting is labeled. Apparent free energies ( $\Delta G_{app}$ ) and enthalpies ( $\Delta H_{app}$ ) in  $\text{kJ mol}^{-1}$ , and entropies ( $\Delta S_{app}$ ) in  $\text{J mol}^{-1} \text{K}^{-1}$ , are shown relative to an adsorbed methanol. Intrinsic free energy barriers ( $\Delta G_{int}$ ) are shown in  $\text{kJ mol}^{-1}$ . The 8-MR (orange, green) and 6-MR (blue) adjacent to each transition state are highlighted.

methanol present. These decreases in the intrinsic barriers propagate to apparent free energy barriers (1 bar, 415 K) for this reaction, indicating that this reaction is more facile at high methanol coverages.

The associative route can also occur in the presence of spectating methanol molecules (Fig. 15). One spectating methanol molecule at these conditions reduces both the overall ( $95 \text{ kJ mol}^{-1}$ ) and intrinsic ( $121 \text{ kJ mol}^{-1}$ ) DME formation barriers by 18 and  $16 \text{ kJ mol}^{-1}$ , respectively. The first spectating methanol prefers to insert between the methanol accepting the methyl group and the

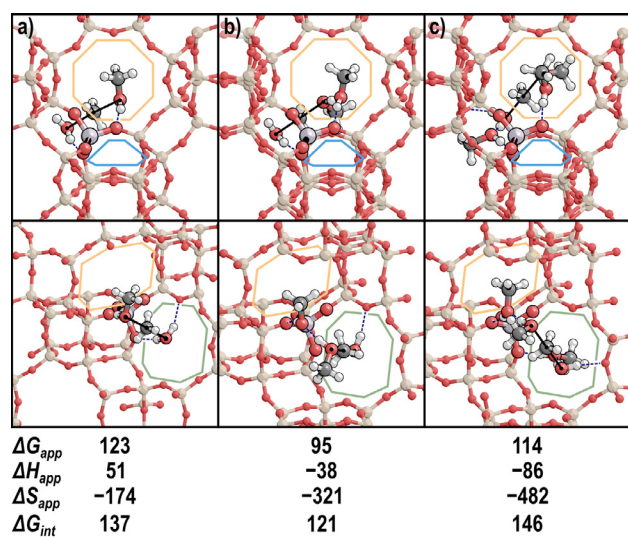


**Fig. 15.** The most favorable transition states for the associative route with (a) zero, (b) one and (c) two spectating  $\text{CH}_3\text{OH}$  molecules. Incipient and breaking bonds of the transition state are shown with black lines and H-bonds in navy. Overall free energies ( $\Delta G_{app}$ ) and enthalpies ( $\Delta H_{app}$ ) in  $\text{kJ mol}^{-1}$ , and entropies ( $\Delta S_{app}$ ) in  $\text{J mol}^{-1} \text{K}^{-1}$ , are shown relative to an adsorbed methanol. Intrinsic free energy barriers ( $\Delta G_{int}$ ) are shown in  $\text{kJ mol}^{-1}$ . The 8-MR (orange, green) and 6-MR (blue) adjacent to each transition state are highlighted.

conjugate base (Fig. 15b). An additional spectating methanol then interacts with the conjugate base between the  $\text{H}_2\text{O}$  leaving group and the conjugate base, such that the transition state only interacts with the framework through spectating methanol molecules (Fig. 15c). This implies that the surface Brønsted acid site is no longer directly involved in the reaction, but instead allows for the formation of protonated clusters within which reactions proceed. These associative transition states occur with lower apparent free energy barriers (1 bar, 415 K) than dissociative transition states at corresponding methanol coverages. Specifically, the associative route with one spectating methanol has the lowest apparent free energy barrier for DME formation ( $95 \text{ kJ mol}^{-1}$ ) of all the transition states tested in this work (Fig. 15b). This indicates that methanol dehydration at sufficiently high pressures and low temperatures will prefer to occur in the presence of spectating methanol molecules and from larger clusters of methanol.

Spectating methanol molecules introduce additional possible pathways that may occur in parallel to form DME (Scheme S.4 in Supp. Info.) and maximum rate analysis can be used to identify quasi-equilibrated and kinetically relevant elementary steps and compare predicted rates of these competing pathways by calculating relevant standard-state rate and equilibrium constants from predicted reaction and activation free energies. This analysis allows for estimation of the contribution of each mechanism tested here (dissociative and associative with 0–3 spectating  $\text{CH}_3\text{OH}$ ) to the overall rates of methanol dehydration measured at different conditions. The associative mechanism with no spectating methanol molecules occurs faster than the same mechanism with one or two spectators at  $<0.02 \text{ kPa CH}_3\text{OH}$  (Fig. 16a); at higher pressures, the rate with one spectating methanol is higher than with zero or two spectators. Fig. 16c shows the best associative pathways (0 spectators  $<0.02 \text{ kPa}$  and 1 spectator at higher pressures) and the best rates of the second step of the dissociative pathway, as well as the rates of the first step of the dissociative pathway with 0–3 spectators. The second step of the dissociative mechanism is rapid at all conditions, and always more so than the first step, regardless of the number of spectating methanol species (Fig. 16c), which indicates that the first step of the dissociative mechanism is the kinetically relevant step for dissociative DME formation at all relevant pressures at 415 K. Overall, the dissociative mechanism without spectators prevails at methanol pressures  $<0.3 \text{ kPa}$ , because rates of associative DME formation are suppressed at such low coverages of methanol dimer and trimer complexes, yet the associative mechanism with one spectating methanol prevails at all methanol partial pressures above  $0.3 \text{ kPa}$  shown here (up to  $100 \text{ kPa}$ ) (Fig. 16c). The high-pressure mechanism implied by studies on heteropolyacids and other zeolite frameworks is that DME is made from the rearrangement of a protonated methanol dimer [10,13,15]; in CHA, this route (absent spectators) does not prevail at any condition. Despite the preferable formation of tetramers and pentamers at higher methanol pressures at 415 K, routes with 2–3 spectators (up to four methanol molecules total) occur at rates slower than the associative route with one spectating methanol. This preference for the associative DME formation route with one spectating methanol, at conditions where tetramers and pentamers begin to increase in coverage, results in apparent kinetic inhibition as methanol molecules must desorb first for the preferred route to occur.

The sum of estimated rates of all parallel pathways (Eq. S.47) that form DME is compared to experimentally measured rates of methanol dehydration at 415 K from  $0.01$  to  $100 \text{ kPa CH}_3\text{OH}$  in Fig. 17. To exemplify qualitative trends, DFT-predicted rates are multiplied by a factor of 5.1 such that their relative scales are similar. The predicted rate behavior agrees qualitatively with that measured in kinetic experiments. Theoretically predicted and experimentally measured rates increase in a first-order regime at

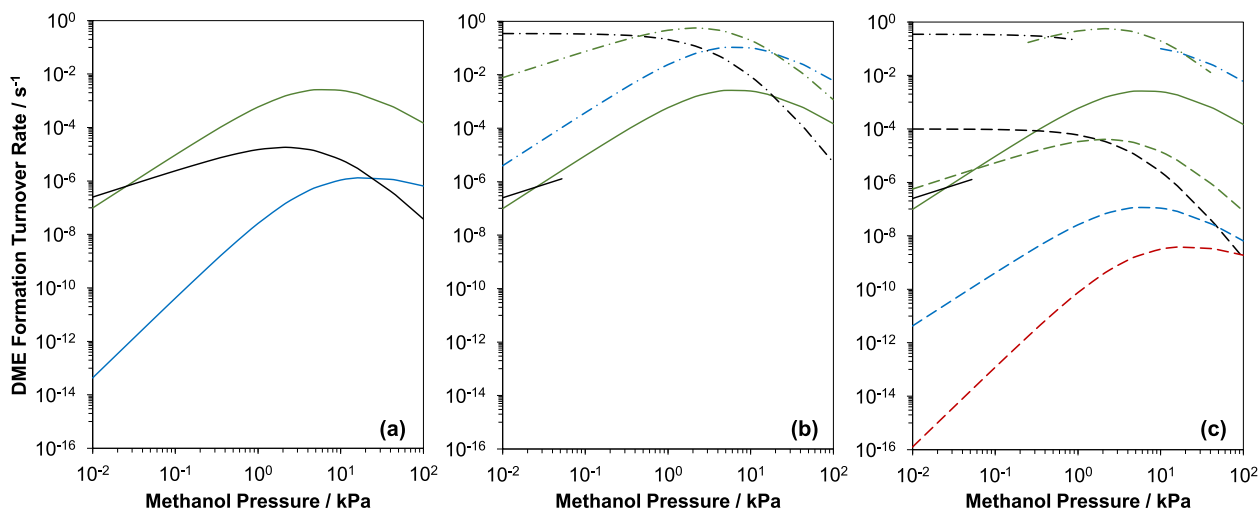


**Fig. 16.** DFT-predicted rates (415 K) with zero (black), one (green), two (blue), or three (red) spectating methanol molecules for (a) the associative mechanism (solid lines), (b) kinetically-relevant DME formation of the dissociative mechanism (dashed-dotted lines), and (c) kinetically-relevant methoxy formation of the dissociative mechanism (dashed lines) at 0.1%  $\text{CH}_3\text{OH}$  conversion. The maximum predicted rates of the associative mechanism (solid lines) are shown in (b) and (c) and of kinetically-relevant DME formation of the dissociative mechanism (dashed-dotted lines) are shown in (c) for comparison.

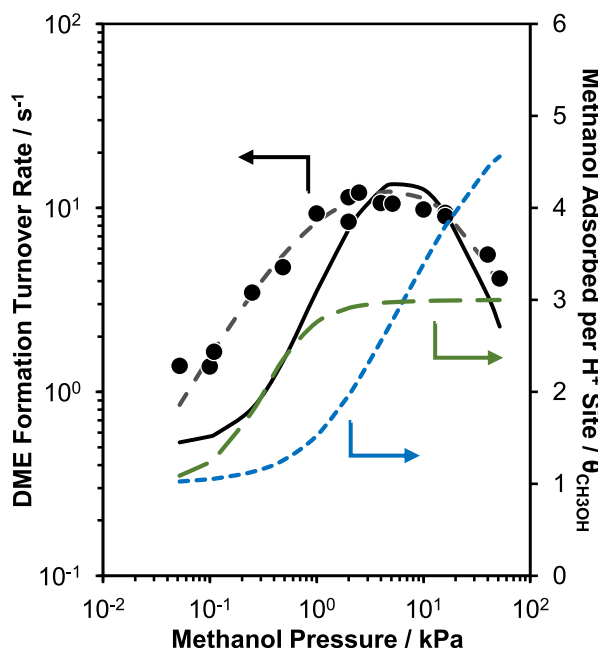


**Fig. 17.** Measured DME formation rates (415 K, per  $\text{H}^+$ ; circles), regression of measured rates to Eq. (12) (grey dashed line), and DFT-predicted rates (415 K) scaled by 5.1x (solid black line, Eq. S.47) at 0.1% conversion. Average methanol cluster size (blue dashed line) and average number of methanol molecules in dehydration transition states (green dashed line) are shown for comparison.

low pressures, reach a maximum corresponding to the zero-order regime, and then become inhibited at higher pressures.

This theoretical evidence in conjunction with spectroscopic and adsorption data (Sections 3.3 and 3.4) indicates that associative methanol dehydration is inhibited at high pressures when trimers, tetramers, and pentamers form in small-pore zeolites. Methanol dehydration preferentially occurs from a trimer containing one spectating methanol at intermediate pressures. Tetramers and pentamers form at higher methanol pressures, but their dehydration transition states are crowded by spectating species and associative routes with only one spectator continue to prevail. Thus, desorption precedes DME formation to yield more favorable

transition states and rates are inhibited at high methanol partial pressures. Given that DME formation proceeds predominantly via the associative route with one spectating methanol at relevant pressures ( $>0.3$  kPa  $\text{CH}_3\text{OH}$ ) and larger clusters can form within the CHA pores, DME formation rates can be described as

$$r_{\text{DME}} = \frac{k_{\text{DME,A3}}K_{\text{D}}K_{\text{Tr}}P_{\text{CH}_3\text{OH}}^2}{1 + K_{\text{D}}P_{\text{CH}_3\text{OH}} + K_{\text{D}}K_{\text{Tr}}P_{\text{CH}_3\text{OH}}^2 + K_{\text{D}}K_{\text{Tr}}K_{\text{Te}}P_{\text{CH}_3\text{OH}}^3 + K_{\text{D}}K_{\text{Tr}}K_{\text{Te}}K_{\text{P}}P_{\text{CH}_3\text{OH}}^4} \quad (12)$$

This rate law reflects the dominance of the associative route with one spectating methanol, and up to a methanol pentamer as potential MASI, and accurately predicts the kinetic behavior measured experimentally (dashed line in Fig. 17).

#### 4. Conclusions

A combined experimental and computational approach was used to investigate the mechanistic origin of the high-pressure inhibition of rates of methanol dehydration to dimethyl ether (DME) in small-pore zeolites (CHA, AEI, LEV, LTA), which occurs irrespective of the framework Al or extraframework  $\text{H}^+$  site distribution. CHA zeolites containing isolated  $\text{H}^+$  sites were chosen as the exemplar case in order to simplify mechanistic interpretation of experimentally measured data and to connect experimental data more faithfully to the low Al-content structures modeled by theory ( $\text{Si}/\text{Al} = 35$ ). Identifying the mechanistic origins of high-pressure inhibition first required knowledge of the prevalent reaction mechanisms and kinetically relevant steps for methanol conversion to DME. Experimental measurements of methanol dehydration turnover rate dependences on pressure (0.05–50 kPa) and temperature (403–473 K), and *in situ* IR spectra that monitor prevalent surface intermediates as a function of reaction conditions, provide evidence that methanol dehydration proceeds via the associative mechanism on isolated  $\text{H}^+$  sites in CHA zeolites. These observations were corroborated by DFT calculations that enabled discriminating candidate parallel dehydration pathways from different surface intermediates. Reaction and activation free energies were calculated for the associative and dissociative dehydration mechanisms after systematically identifying the most energetically favorable adsorbate and transition state configurations by reorienting transition states and intermediates around framework binding sites and

within adjacent voids. The most stable transition state structures were those that maximized the number of hydrogen bonds made with framework O atoms, leading to more effective charge distribution and stronger stabilizing interactions between reacting species and the zeolite framework. A maximum rate analysis of the most favorable routes for the associative and dissociative pathways showed that the dissociative mechanism prevails at isolated H<sup>+</sup> sites in CHA at sufficiently low methanol pressures (e.g., <4 kPa at 415 K), but that the associative mechanism dominates at higher pressures, especially those corresponding to the onset of experimentally observed high-pressure inhibition (>10 kPa CH<sub>3</sub>OH, 415 K).

Methanol adsorption equilibrium isotherms (10<sup>-4</sup>–10 kPa, 293 K) were used to estimate the methanol coverages (per H<sup>+</sup> site) present during catalysis (0.05–50 kPa, 415 K), by comparing data at equivalent gaseous methanol free energy. This analysis suggests that inhibition of methanol dehydration rates (415 K) occurs at coverages exceeding 2 CH<sub>3</sub>OH per H<sup>+</sup> site. Methanol dehydration rates measured as a function of temperature (403–473 K) reveal that high-pressure inhibition disappears at elevated temperatures (>450 K), concomitant with the disappearance of methanol clusters in IR spectra measured under equivalent conditions. These experimental data indicate that the associative dehydration mechanism becomes inhibited by the adsorption of excess methanol, but these data alone are unable to distinguish between parallel dehydration pathways that may proceed through different methanol intermediates at different rates.

DFT-predicted methanol coverages agree with those estimated experimentally and indicate that inhibition of methanol dehydration occurs in the presence of methanol trimers and tetramers, with pentamers ultimately forming at the highest of experimental pressures studied (>40 kPa, 415 K). Methanol coverages calculated at high pressures and elevated temperatures (up to 473 K) show that the surface shifts to being covered primarily by methanol dimers, consistent with the disappearance of high-pressure inhibition at temperatures >450 K. Free energies for DME formation transition states were calculated for the associative and dissociative pathways, and a maximum rate analysis was used to predict DME formation rates as a function of methanol pressure and coverage. This analysis indicates that the associative dehydration pathway prevails under the experimental conditions tested here (0.1–50 kPa CH<sub>3</sub>OH, 415 K), but that the most favorable dehydration route occurs via a methanol trimer and that inhibition reflects the formation of methanol tetramers, from which methanol must first desorb to form transition states of sufficient stability. Applying observations from both experiment and theory, a rate expression was derived for the associative dehydration mechanism wherein DME is formed via methanol trimers and becomes inhibited by methanol tetramers, which describes DME formation rates measured experimentally on isolated H<sup>+</sup> sites in CHA. This kinetic model allows for the quantitative description of methanol inhibition in CHA zeolites, and extension of this analysis to better understand the mechanistic differences between isolated and paired H<sup>+</sup> sites in small-pore zeolites. These findings highlight how modeling interactions between transition states and the zeolite framework with different reactant coverages can be used to clarify and extend insights gained from measurements of kinetic inhibition. This work highlights methods for handling the complexity that arises when zeolites turn over catalytic cycles under conditions wherein molecules are present in extended complexes and approach condensation regimes.

## Acknowledgements

We acknowledge financial support provided by the National Science Foundation CAREER program under award number

1552517-CBET for the experimental work at Purdue. We also thank Sachem, Inc. for providing the organic structure-directing agent used to synthesize SSZ-13. A.H. and D.H. also acknowledge funding from the ACS Petroleum Research Fund New Doctoral Investigation Award (57079DNI5). This work used the Extreme Science and Engineering Discovery Environment (XSEDE) [60], which is supported by the National Science Foundation grant number ACI-1548562 through allocation CTS160041. Additional computational resources were provided by the University of Florida Research Computing.

## Appendix A. Supplementary material

Supplementary data to this article can be found online at <https://doi.org/10.1016/j.jcat.2019.10.012>.

## References

- [1] C. Chang, A. Silvestri, The conversion of methanol and other O-compounds to hydrocarbons over zeolite catalysts, *J. Catal.* 47 (1977) 249–259, [https://doi.org/10.1016/0021-9517\(77\)90172-5](https://doi.org/10.1016/0021-9517(77)90172-5).
- [2] R. Dessau, On the H-ZSM-5 catalyzed formation of ethylene from methanol or higher olefins, *J. Catal.* 99 (1986) 111–116, [https://doi.org/10.1016/0021-9517\(86\)90204-6](https://doi.org/10.1016/0021-9517(86)90204-6).
- [3] S. Ilias, A. Bhan, Mechanism of the catalytic conversion of methanol to hydrocarbons, *ACS Catal.* 3 (2013) 18–31, <https://doi.org/10.1021/cs3006583>.
- [4] U. Olsbye, S. Svelle, M. Bjørgen, P. Beato, T.V.W. Janssens, F. Joensen, et al., Conversion of methanol to hydrocarbons: how zeolite cavity and pore size controls product selectivity, *Angew. Chem. Int. Ed. Engl.* 51 (2012) 5810–5831, <https://doi.org/10.1002/anie.201103657>.
- [5] J.H. Kang, F.H. Alshafei, S.I. Zones, M.E. Davis, Cage-defining ring: a molecular sieve structural indicator for light olefin product distribution from the methanol-to-olefins reaction, *ACS Catal.* 9 (2019) 6012–6019, <https://doi.org/10.1021/acscatal.9b00746>.
- [6] P. Bollini, A. Bhan, Improving HSAPO-34 methanol-to-olefin turnover capacity by seeding the hydrocarbon pool, *ChemPhysChem.* 19 (2018) 479–483, <https://doi.org/10.1002/cphc.201701027>.
- [7] Y. Liu, F.M. Kirchberger, S. Müller, M. Eder, M. Tonigold, M. Sanchez-Sanchez, et al., Critical role of formaldehyde during methanol conversion to hydrocarbons, *Nat. Commun.* 10 (2019) 1462, <https://doi.org/10.1038/s41467-019-09449-7>.
- [8] Y. Liu, S. Müller, D. Berger, J. Jelic, K. Reuter, M. Tonigold, et al., Formation mechanism of the first carbon-carbon bond and the first olefin in the methanol conversion into hydrocarbons, *Angew. Chem. Int. Ed. Engl.* 55 (2016) 5723–5726, <https://doi.org/10.1002/anie.201511678>.
- [9] E. Derouane, J. Nagy, P. Dejaifve, J.H.C. van Hooff, B.P. Spekman, J.C. Védrine, et al., Elucidation of the mechanism of conversion of methanol and ethanol to hydrocarbons on a new type of synthetic zeolite, *J. Catal.* 53 (1978) 40–55, [https://doi.org/10.1016/0021-9517\(78\)90006-4](https://doi.org/10.1016/0021-9517(78)90006-4).
- [10] R.T. Carr, M. Neurock, E. Iglesia, Catalytic consequences of acid strength in the conversion of methanol to dimethyl ether, *J. Catal.* 278 (2011) 78–93, <https://doi.org/10.1016/j.jcat.2010.11.017>.
- [11] A.J. Jones, S.I. Zones, E. Iglesia, Implications of transition state confinement within small voids for acid catalysis, *J. Phys. Chem. C.* 118 (2014) 17787–17800, <https://doi.org/10.1021/jp5050095>.
- [12] A.J. Jones, R.T. Carr, S.I. Zones, E. Iglesia, Acid strength and solvation in catalysis by MFI zeolites and effects of the identity, concentration and location of framework heteroatoms, *J. Catal.* 312 (2014) 58–68, <https://doi.org/10.1016/j.jcat.2014.01.007>.
- [13] A.J. Jones, E. Iglesia, Kinetic, spectroscopic, and theoretical assessment of associative and dissociative methanol dehydration routes in zeolites, *Angew. Chem. Int. Ed. Engl.* 53 (2014) 12177–12181, <https://doi.org/10.1002/anie.201406823>.
- [14] R. Gounder, A.J. Jones, R.T. Carr, E. Iglesia, Solvation and acid strength effects on catalysis by faujasite zeolites, *J. Catal.* 286 (2012) 214–223, <https://doi.org/10.1016/j.jcat.2011.11.002>.
- [15] A. Ghorbanpour, J.D. Rimer, L.C. Grabow, Computational assessment of the dominant factors governing the mechanism of methanol dehydration over H-ZSM-5 with heterogeneous aluminum distribution, *ACS Catal.* 6 (2016) 2287–2298, <https://doi.org/10.1021/acscatal.5b02367>.
- [16] J.R. Di Iorio, C.T. Nimlos, R. Gounder, Introducing catalytic diversity into single-site chabazite zeolites of fixed composition via synthetic control of active site proximity, *ACS Catal.* 7 (2017) 6663–6674, <https://doi.org/10.1021/acscatal.7b01273>.
- [17] J.R. Di Iorio, R. Gounder, Controlling the isolation and pairing of aluminum in chabazite zeolites using mixtures of organic and inorganic structure-directing agents, *Chem. Mater.* 28 (2016) 2236–2247, <https://doi.org/10.1021/acs.chemmater.6b00181>.
- [18] S. Nystrom, A. Hoffman, D. Hibbits, Tuning Brønsted acid strength by altering site proximity in CHA framework zeolites, *ACS Catal.* 8 (2018) 7842–7860, <https://doi.org/10.1021/acscatal.8b02049>.



- [19] H. Chiang, A. Bhan, Catalytic consequences of hydroxyl group location on the rate and mechanism of parallel dehydration reactions of ethanol over acidic zeolites, *J. Catal.* 271 (2010) 251–261, <https://doi.org/10.1016/j.jcat.2010.01.021>.
- [20] Y. Zhi, H. Shi, L. Mu, Y. Liu, D. Mei, D.M. Camaioni, et al., Dehydration pathways of 1-Propanol on HZSM-5 in the presence and absence of water, *J. Am. Chem. Soc.* 137 (2015) 15781–15794, <https://doi.org/10.1021/jacs.5b09107>.
- [21] J. Macht, M.J. Janik, M. Neurock, E. Iglesia, Mechanistic consequences of composition in acid catalysis by polyoxometalate Keggin clusters, *J. Am. Chem. Soc.* 130 (2008) 10369–10379, <https://doi.org/10.1021/ja803114r>.
- [22] M. Dusselier, J.E. Schmidt, R. Moulton, B. Haymore, M. Hellums, M.E. Davis, Influence of organic structure directing agent isomer distribution on the synthesis of SSZ-39, *Chem. Mater.* 27 (2015) 2695–2702, <https://doi.org/10.1021/acs.chemmater.5b00651>.
- [23] J.D. Albarracín-Caballero, I. Khurana, J.R. Di Iorio, A.J. Shih, J.E. Schmidt, M. Dusselier, et al., Structural and kinetic changes to small-pore Cu-zeolites after hydrothermal aging treatments and selective catalytic reduction of NO<sub>x</sub> with ammonia, *React. Chem. Eng.* 2 (2017) 168–179, <https://doi.org/10.1039/C6RE00198J>.
- [24] S. Shibata, M. Itakura, Y. Ide, M. Sadakane, T. Sano, FAU-LEV interzeolite conversion in fluoride media, *Micropor. Mesopor. Mat.* 138 (2011) 32–39, <https://doi.org/10.1016/j.micromeso.2010.09.034>.
- [25] D. Jo, T. Ryu, G.T. Park, P.S. Kim, C.H. Kim, I.-S. Nam, et al., Synthesis of high-silica LTA and UFI zeolites and NH<sub>3</sub>-SCR performance of their copper-exchanged form, *ACS Catal.* 6 (2016) 2443–2447, <https://doi.org/10.1021/acscatal.6b00489>.
- [26] C. Baerlocher, L.B. McCusker, Database of Zeolite Structures: <http://www.iza-structure.org/databases>, (2013), <http://www.iza-structure.org/databases>.
- [27] J.R. Di Iorio, S.A. Bates, A.A. Verma, W.N. Delgass, F.H. Ribeiro, J.T. Miller, et al., The dynamic nature of brønsted acid sites in Cu-Zeolites during NO<sub>x</sub> selective catalytic reduction: quantification by gas-phase ammonia titration, *Top. Catal.* 58 (2015) 424–434, <https://doi.org/10.1007/s11244-015-0387-8>.
- [28] V.J. Cybulskis, J.W. Harris, Y. Zvinevich, F.H. Ribeiro, R. Gounder, A transmission infrared cell design for temperature-controlled adsorption and reactivity studies on heterogeneous catalysts, *Rev. Sci. Instrum.* 87 103101 (2016), <https://doi.org/10.1063/1.4963665>.
- [29] J.W. Harris, M.J. Cordon, J.R. Di Iorio, J.C. Vega-Vila, F.H. Ribeiro, R. Gounder, Titration and quantification of open and closed Lewis acid sites in Sn-Beta zeolites that catalyze glucose isomerization, *J. Catal.* 335 (2016) 141–154, <https://doi.org/10.1016/j.jcat.2015.12.024>.
- [30] J.S. Bates, R. Gounder, Influence of confining environment polarity on ethanol dehydration catalysis by Lewis acid zeolites, *J. Catal.* 365 (2018) 213–226, <https://doi.org/10.1016/j.jcat.2018.05.009>.
- [31] G. Kresse, J. Hafner, Ab initio molecular-dynamics simulation of the liquid-metal-amorphous-semiconductor transition in germanium, *Phys. Rev. B. Condens. Matter.* 49 (1994) 14251–14269, <https://doi.org/10.1103/PhysRevB.49.14251>.
- [32] G. Kresse, J. Hafner, Ab initio molecular dynamics for liquid metals, *Phys. Rev. B.* 47 (1993) 558–561, <https://doi.org/10.1103/PhysRevB.47.558>.
- [33] G. Kresse, J. Furthmüller, Efficient iterative schemes for ab initio total-energy calculations using a plane-wave basis set, *Phys. Rev. B.* 54 (1996) 11169–11186, <https://doi.org/10.1103/PhysRevB.54.11169>.
- [34] G. Kresse, J. Furthmüller, Efficiency of ab-initio total energy calculations for metals and semiconductors using a plane-wave basis set, *Comp. Mater. Sci.* 6 (1996) 15–50, [https://doi.org/10.1016/0927-0256\(96\)00008-0](https://doi.org/10.1016/0927-0256(96)00008-0).
- [35] P. Kravchenko, C. Plaisance, D. Hibbitts, A new computational interface for catalysis, Pre-Print Available [rxiv.link/8040737](https://doi.org/10.26434/chemrxiv.8040737.v3) (n.d.), <https://doi.org/10.26434/chemrxiv.8040737.v3>.
- [36] G. Kresse, D. Joubert, From ultrasoft pseudopotentials to the projector augmented-wave method, *Phys. Rev. B.* 59 (1999) 1758–1775, <https://doi.org/10.1103/PhysRevB.59.1758>.
- [37] P.E. Blöchl, Projector augmented-wave method, *Phys. Rev. B.* 50 (1994) 17953–17979, <https://doi.org/10.1103/PhysRevB.50.17953>.
- [38] J.P. Perdew, K. Burke, M. Ernzerhof, Generalized gradient approximation made simple, *Phys. Rev. Lett.* 77 (1996) 3865–3868, <https://doi.org/10.1103/PhysRevLett.77.3865>.
- [39] S. Grimme, S. Ehrlich, L. Goerigk, Effect of the damping function in dispersion corrected density functional theory, *J. Comput. Chem.* 32 (2011) 1456–1465, <https://doi.org/10.1002/jcc.21759>.
- [40] S. Grimme, J. Antony, S. Ehrlich, H. Krieg, A consistent and accurate ab initio parametrization of density functional dispersion correction (DFT-D) for the 94 elements H-Pu, *J. Chem. Phys.* 132 (2010) 154104, <https://doi.org/10.1063/1.3382344>.
- [41] G. Henkelman, H. Jónsson, Improved tangent estimate in the nudged elastic band method for finding minimum energy paths and saddle points, *J. Chem. Phys.* 113 (2000) 9978–9985, <https://doi.org/10.1063/1.1323224>.
- [42] H. Jónsson, G. Mills, K.W. Jacobsen, Nudged elastic band method for finding minimum energy paths of transitions, in: B.J. Berne, G. Ciccotti, D.F. Coker (Eds.), *Classical and Quantum Dynamics in Condensed Phase Simulations*, World Scientific, 1998, pp. 385–404, [https://doi.org/10.1142/9789812839664\\_0016](https://doi.org/10.1142/9789812839664_0016).
- [43] G. Henkelman, H. Jónsson, A dimer method for finding saddle points on high dimensional potential surfaces using only first derivatives, *J. Chem. Phys.* 111 (1999) 7010–7022, <https://doi.org/10.1063/1.480097>.
- [44] A.J. Jones, E. Iglesia, The strength of brønsted acid sites in microporous aluminosilicates, *ACS Catal.* 5 (2015) 5741–5755, <https://doi.org/10.1021/acscatal.5b01133>.
- [45] A. Hoffman, M. DeLuca, D. Hibbitts, Restructuring of MFI framework zeolite models and their associated artifacts in density functional theory calculations, *J. Phys. Chem. C.* 123 (2019) 6572–6585, <https://doi.org/10.1021/acs.jpcc.8b12230>.
- [46] D.A. McQuarrie, *Statistical Mechanics*, University Science Books, Sausalito, Calif, 2000.
- [47] S. Herrmann, E. Iglesia, Elementary steps in acetone condensation reactions catalyzed by aluminosilicates with diverse void structures, *J. Catal.* 346 (2017) 134–153, <https://doi.org/10.1016/j.jcat.2016.12.011>.
- [48] M. DeLuca, P. Kravchenko, A. Hoffman, D. Hibbitts, Mechanism and Kinetics of Methylating C6–C12 Methylbenzenes with Methanol and Dimethyl Ether in H-MFI Zeolites, *ACS Catal.* 9 (2019) 6444–6460, <https://doi.org/10.1021/acscatal.9b00650>.
- [49] R. Gounder, E. Iglesia, The catalytic diversity of zeolites: confinement and solvation effects within voids of molecular dimensions, *Chem. Commun.* 49 (2013) 3491–3509, <https://doi.org/10.1039/c3cc40731d>.
- [50] S. Wang, E. Iglesia, Catalytic diversity conferred by confinement of protons within porous aluminosilicates in Prins condensation reactions, *J. Catal.* 352 (2017) 415–435, <https://doi.org/10.1016/j.jcat.2017.06.012>.
- [51] G. Mirth, J.A. Lercher, M.W. Anderson, J. Klinowski, Adsorption complexes of methanol on zeolite ZSM-5, *Faraday Trans.* 86 (1990) 3039–3044, <https://doi.org/10.1039/ft9908603039>.
- [52] C.A. Farberow, J.A. Dumesic, M. Mavrikakis, Density functional theory calculations and analysis of reaction pathways for reduction of nitric oxide by hydrogen on Pt(111), *ACS Catal.* 4 (2014) 3307–3319, <https://doi.org/10.1021/cs500668k>.
- [53] P. Deshlahra, R.T. Carr, E. Iglesia, Ionic and covalent stabilization of intermediates and transition states in catalysis by solid acids, *J. Am. Chem. Soc.* 136 (2014) 15229–15247, <https://doi.org/10.1021/ja506149c>.
- [54] P. Deshlahra, R.T. Carr, S.-H. Choi, E. Iglesia, Mechanistic details and reactivity descriptors in oxidation and acid catalysis of methanol, *ACS Catal.* 5 (2015) 666–682, <https://doi.org/10.1021/cs501599y>.
- [55] P.L. Llewellyn, E. Bloch, S. Bourrelly, Surface area/porosity, adsorption, diffusion, in: M. Che, J.C. Védrine (Eds.), *Characterization of Solid Materials and Heterogeneous Catalysts: From Structure to Surface Reactivity*, Wiley-VCH Verlag GmbH & Co. KGaA, Weinheim, Germany, 2012, pp. 853–879, <https://doi.org/10.1002/9783527645329.ch19>.
- [56] M. Thommes, Physical adsorption characterization of nanoporous materials, *Chemie Ingenieur Technik.* 82 (2010) 1059–1073, <https://doi.org/10.1002/cite.201000064>.
- [57] W.S. Borghard, P.T. Reischman, E.W. Sheppard, Argon Sorption in ZSM-5, *J. Catal.* 139 (1993) 19–23, <https://doi.org/10.1006/jcat.1993.1002>.
- [58] W. Knaeble, E. Iglesia, Kinetic and theoretical insights into the mechanism of Alkanol dehydration on solid Brønsted acid catalysts, *J. Phys. Chem. C.* 120 (2016) 3371–3389, <https://doi.org/10.1021/acs.jpcc.5b11127>.
- [59] T.J. Wilke, M.A. Barteau, Cation exchange effects on methanol oxidation and dehydration by supported polyoxometalates, *J. Catal.* 371 (2019) 357–367, <https://doi.org/10.1016/j.jcat.2019.02.006>.
- [60] J. Towns, T. Cockerill, M. Dahan, I. Foster, K. Gauthier, A. Grimshaw, et al., XSEDE: accelerating scientific discovery, *Comput. Sci. Eng.* 16 (2014) 62–74, <https://doi.org/10.1109/MCSE.2014.80>.